Electrocatalytic amplification of coreactant electrochemiluminescence using redox mediators

Sara Knežević, Emily Kerr, Giovanni Valenti, Francesco Paolucci, Paul S Francis, Conor F Hogan, Neso Sojic, Frédéric Kanoufi

Electrochimica Acta 499 (2024) 144677

Contents lists available at ScienceDirect

Electrochimica Acta

journal homepage: www.journals.elsevier.com/electrochimica-acta

Electrocatalytic amplification of coreactant electrochemiluminescence using redox mediators

Sara Knežević [a], Emily Kerr [b], Giovanni Valenti [c], Francesco Paolucci [c], Paul S. Francis [d], Conor F. Hogan [e], Neso Sojic [a], Frédéric Kanoufi [f,*]

[a] Univ. Bordeaux, CNRS, Bordeaux INP, Institut des Sciences Moléculaires, UMR 5255 33607 Pessac, France
[b] Institute for Frontier Materials, Deakin University, Geelong, Victoria 3220, Australia
[c] Department of Chemistry Giacomo Ciamician, University of Bologna, via Selmi 2, Bologna 40126, Italy
[d] Deakin University, Centre for Sustainable Bioproducts, Faculty of Science, Engineering and Built Environment, Geelong, Victoria 3220, Australia
[e] Department of Biochemistry and Chemistry, Biomedical and Environmental Sensor Technology Centre, La Trobe Institute for Molecular Science, La Trobe University, Melbourne, Victoria 3086, Australia
[f] Université Paris Cité, ITODYS, CNRS F-75013 Paris, France

ARTICLE INFO

Keywords:
Electrochemiluminescence
Molecular electrocatalysis
Redox mediator
Reaction mechanism
Simulation

ABSTRACT

Electrochemiluminescence (ECL) has emerged as a sensitive analytical technique with a wide range of applications. While recent studies have begun to explore the role of redox mediators to facilitate ECL systems, this work extends these foundational insights by developing a comprehensive theoretical framework that supports, generalizes, and rationalizes mechanistic pathways borrowed from molecular electrocatalysis. This advancement is demonstrated through the electrocatalytic amplification of coreactant ECL within the $[Ru(bpy)_3]^{2+}$/TPrA system, utilizing a water-soluble redox-active Ir(III) complex as an electrocatalyst. Our investigation unveils previously uncharted mechanisms that enable the enhancement of Ru complex ECL at low electrode potentials, crucially without requiring the direct oxidation of $[Ru(bpy)_3]^{2+}$ or TPrA at the electrode, thus offering a deeper understanding of ECL activation through moelcular electrocatalysis. Through an integrated approach combining electrochemical analysis, spectroscopic investigation, and finite element modeling, we elucidate how the redox mediator critically modulates ECL efficiency by controlling the kinetics of radical species production and decay. The mediation by the Ir(III) complex not only governs the generation of TPrA radicals and excited $[Ru(bpy)_3]^{2+}$ states, thereby enhancing ECL intensity, but also the conditions under which ECL can be quenched. Further exploration of the mediator's redox characteristics provides predictive insights into ECL behavior, underscoring the mediator's redox potential as pivotal in determining ECL onset, peak potential, and intensity. This refined understanding paves the way for tailoring ECL systems for enhanced performance in analytical, imaging, and biomedical applications through the judicious selection of redox mediators.

1. Introduction

Electrochemiluminescence (ECL) is the light-emission process that occurs when an excited state of a luminophore is populated through a highly exergonic electron transfer reaction of electrogenerated intermediates [1]. ECL, known for its high sensitivity, negligible background luminescence, and excellent spatiotemporal resolution, has found diverse applications[2–4] in bioanalysis [5–11], imaging of single cells[12–16] and single molecules [17–19], studying collisions [20–22], phase boundaries[23–25] and catalytic sites [26–28]. The most common, and useful mode of ECL is coreactant ECL, which consists of a luminophore and a sacrificial coreactant, allowing the production of light with a single applied potential in aqueous solutions. The majority of ECL applications are based on the tris(2,2′-bipyridine)ruthenium(II) ($[Ru(bpy)_3]^{2+}$) luminophore and tri-*n*-propylamine (TPrA) coreactant system, due to its efficient, stable and reproducible ECL emission, which can be generated at moderate electrochemical potentials in aqueous media.

ECL of $[Ru(bpy)_3]^{2+}$/TPrA can be generated through the 'homogeneous' route, so called because the luminophore and the coreactant are free in solution. In this case, direct electrooxidation of the luminophore occurs generally at the electrode surface, followed by electron transfer

* Corresponding author.
E-mail address: frederic.kanoufi@u-paris.fr (F. Kanoufi).

https://doi.org/10.1016/j.electacta.2024.144677
Received 22 March 2024; Received in revised form 4 June 2024; Accepted 4 July 2024
Available online 7 July 2024

between its oxidized state ($[Ru(bpy)_3]^{3+}$) and a potent reductant ($TPrA^{\bullet}$) formed from the oxidation and deprotonation of TPrA. This leads to the population of luminophore's excited state, resulting in ECL emission [29]. Another ECL pathway, important for bioanalysis and microscopy, is called the 'heterogeneous' or 'remote' route (Fig. 1A), which implies that the luminophore is not oxidized directly by the electrode. This is the case, for instance, when the luminophore is immobilized on a non-conducting entity such as an insulating polystyrene bead or a living cell. Nevertheless, this pathway can also occur when $[Ru(bpy)_3]^{2+}$ is free in solution, by applying potentials sufficient to oxidize the coreactant but not the luminophore. Under both of these conditions, $[Ru(bpy)_3]^{2+}$ is not oxidized at the electrode surface. Instead, $TPrA^{\bullet}$ reduces $[Ru(bpy)_3]^{2+}$ to $[Ru(bpy)_3]^{+}$, and ECL is produced upon its subsequent reaction with the radical cation $TPrA^{\bullet+}$ initially formed by oxidation of TPrA.

Generally, the only oxidant in the $[Ru(bpy)_3]^{2+}$/TPrA coreactant system operating through the 'remote' route (Fig. 1A) is the short-lived $TPrA^{\bullet+}$ (with a half-life time of ~200 μs) [29–31]. This mechanistic pathway enables $[Ru(bpy)_3]^{2+}$ derivatives to be used as labels, rendering this coreactant system indispensable in biological assays and ECL imaging. Nevertheless, the efficiency of ECL generation is constrained by the short half-life of $TPrA^{\bullet+}$, thereby limiting the thickness of the ECL-emitting layer and the ECL signal [31]. To overcome this limitation, extensive investigation has been focused on fine-tuning the reaction route, through the development of nanomaterials [32–35], luminophores [36–41], or coreactants [42–45], with improved properties. However, the success of these approaches strongly depends on a comprehensive mechanistic understanding of the ECL system [29,30,46–49].

Recently, iridium complexes have emerged as promising luminophores, offering various ECL onset redox potentials and emission colours [39,41,50–54]. In a study by Kerr et al. [55], ten-fold enhancement of $[Ru(bpy)_3]^{2+}$ ECL emission was reported in the presence of TPrA and the freely diffusing, redox-active tris(2-(2-pyridinyl-κ*N*)−4-sulfonatophenyl-κ*C*)iridium(III) ($[Ir^{III}(sppy)_3]^{3-}$) complex. This enhancement was attributed to the improved efficiency of this mixed coreactant system with $[Ir^{IV}(sppy)_3]^{2-}$ (rather than $TPrA^{\bullet+}$) acting as the main mediator for oxidative generation of the excited state from $[Ru(bpy)_3]^{+}$, as depicted in Fig. 1C. In addition to the increased intensity, the study also reported a shift of $[Ru(bpy)_3]^{2+}$ ECL towards lower overpotentials. Finally, the $[Ir^{III}(sppy)_3]^{3-}$ ECL emission, generated through the oxidation–reduction mechanism (Fig. 1B), can be used for internal standardization of the coreactant ECL of $[Ru(bpy)_3]^{2+}$. The chemical structure of this Ir(III) complex is shown in Fig. S1.

The potential of this mixed coreactant system was demonstrated not only in the original publication but also in subsequent studies addressing its value in the context of ECL bioassays [56] and cell imaging [14]. Furthermore, Fracassa et al. [57]. demonstrated experimentally that in such $[Ru(bpy)_3]^{2+}$-immobilized configuration, redox mediators in solutions, such as Ir complexes, can modulate the ECL of $[Ru(bpy)_3]^{2+}$/TPrA coreactant system, either by quenching or by enhancing it based on their redox properties. Redox mediators with reduction potentials equal to or more positive than that of $TPrA^{\bullet}$ scavenge radical species and quench ECL, while those with easily accessible oxidation potentials boost ECL by homogenously oxidizing $[Ru(bpy)_3]^{+}$ and TPrA (Fig. 1C). We recently postulated that another condition for enhancing the intensity of the $[Ru(bpy)_3]^{2+}$/TPrA ECL at low anodic potentials could be that the redox mediator can also mediate the oxidation of the TPrA coreactant (Fig. 1**D**) [56–58]. This situation is reminiscent of molecular electrocatalysis pathways where a catalyst is used to trigger electrochemical reactions in solution [59,60]. Here, using $[Ir^{III}(sppy)_3]^{3-}$ as a molecular redox mediator, we expect oxidation of both the coreactant and $[Ru(bpy)_3]^{2+}$ by the electro-oxidized form of the mediator, $[Ir^{IV}(sppy)_3]^{2-}$, without the need to oxidize the other reactants directly at the electrode. We have showed that the oxidation of $[Ir^{III}(sppy)_3]^{3-}$ at moderate potentials (ca. 0.81 V) effectively enhances

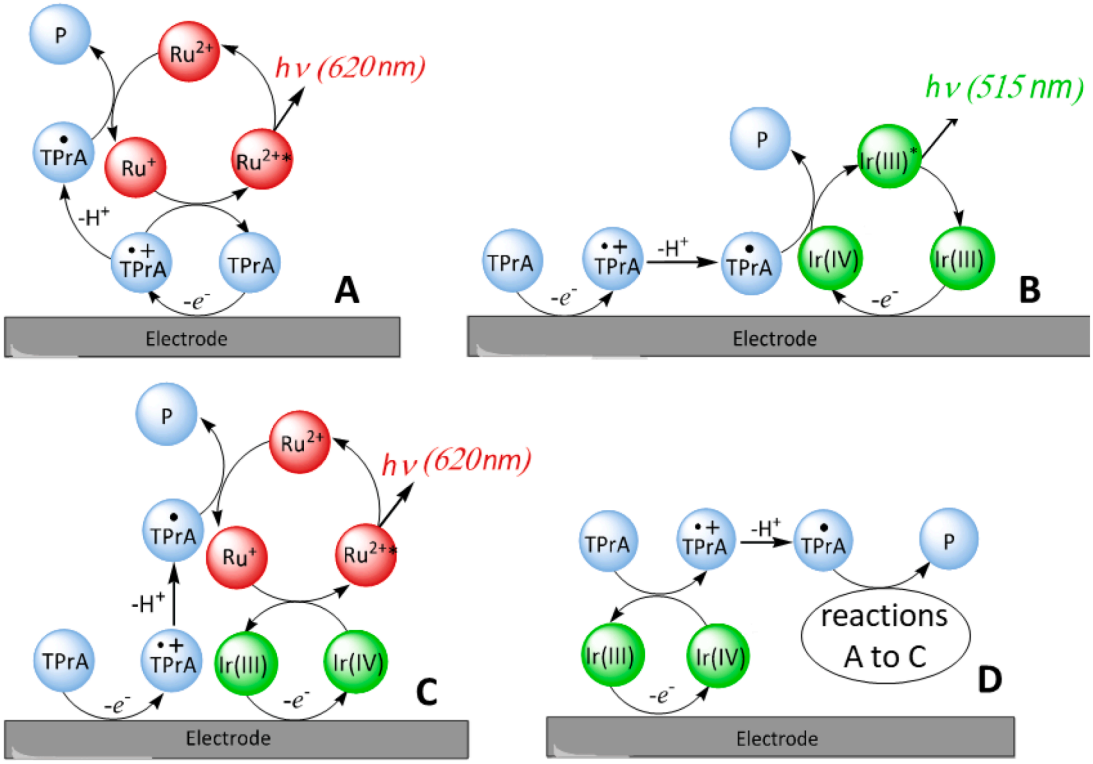

Fig. 1. Schematics of the **(A)** conventional 'remote' ECL route, **(B)** direct route to $[Ir^{III}(sppy)_3]^{3-}$ ECL, **(C)** enhanced 'redox-mediated' ECL route and **(D)** redox catalysis (catalytic oxidation of TPrA by $[Ir^{IV}(sppy)_3]^{2-}$). Ru^{2+}, Ir(III) and TPrA represent the $[Ru(bpy)_3]^{2+}$ luminophore, the $[Ir^{III}(sppy)_3]^{3-}$ redox mediator and tri-*n*-propylamine, respectively.

the co-reactant ECL of $[Ru(bpy)_3]^{2+}$ [56–58]. However, a clear contribution of this electrocatalytic path in the mechanism supporting enhanced ECL of $[Ru(bpy)_3]^{2+}$ in the presence of $[Ir^{III}(sppy)_3]^{3-}$ and TPrA remains absent.

Here, we initially integrated these two electrocatalytic mechanistic paths into finite element simulations and tested how they reproduce different electrochemical and ECL experiments, to systematically study the role of the Ir(III) electrocatalytic mediator within the coreactant ECL mechanism. The results align with prior research, suggesting that, despite the complexity of the mixed luminophore system, amplified low potential ECL emission primarily arises from three kinetically limited reactions that modulate the concentration ratio of oxidant ($TPrA^{+\bullet}$, $[Ir^{IV}(sppy)_3]^{2-}$) and reductant ($TPrA^{\bullet}$) radical species. Specifically, the homogenous oxidation reactions facilitated by electrogenerated $[Ir^{IV}(sppy)_3]^{2-}$ species produce TPrA radicals and the $[Ru(bpy)_3]^{2+*}$ excited state at low anodic overpotentials (Fig. 1D and 1C, respectively), shifting both onset and peak $[Ru(bpy)_3]^{2+}$ ECL to around 300 mV less positive potentials. Conversely, the reaction between $[Ir^{IV}(sppy)_3]^{2-}$ and $TPrA^{\bullet}$ (Fig. 1B) depletes both positive and neutral TPrA radicals, quenching $[Ru(bpy)_3]^{2+}$ ECL. This indirect ECL quenching elucidates the experimental findings [55,57,58] indicating that the intensity of $[Ru(bpy)_3]^{2+}$ ECL does not directly correlate with the concentration of the redox mediator. Optimal enhancement is observed at approximately 100 μM $[Ir^{IV}(sppy)_3]^{2-}$, beyond which further increases in the mediator's concentration diminish the enhancement and even quench the ECL emission of $[Ru(bpy)_3]^{2+}$.

This study sheds light not only on the dynamics of ECL generation and its spatial extension in the mixed luminophore system, but also the interplay between specific mechanistic steps, revealing the links between the ECL properties and electrochemical characteristics of a redox mediator and providing insight for future studies and applications.

2. Experimental section

2.1. Reagents and apparatus

Reagents and solvents were purchased from commercial suppliers and used without further purification. $[Ir^{III}(sppy)_3]^{3-}$ was purchased from Lumtec as a custom synthesis based on synthetic details previously described [55,61]. Tris(2,2′-bipyridine)ruthenium(II) dichloride hexahydrate ($[Ru(bpy)]_3Cl_2{\cdot}6H_2O$) was purchased from Strem (USA). Potassium phosphate monobasic and dibasic salt, sodium chloride, TPrA and *fac*-$Ir(ppy)_3$ were purchased from Sigma-Aldrich Australia.

2.2. Electrochemistry and ECL

We used a previously described custom cell design [27] with glassy carbon working electrode, platinum wire counter (CH Instruments) and leakless Ag/AgCl reference (model ET069; eDAQ Australia) to collect all electrochemical and ECL data. The glassy carbon electrode was polished using 1 μm and 0.05 μm alumina polishing powder (CH Instruments) followed by sonication in ethanol prior to each experiment. An Autolab PGSTAT204 or Autolab PGSTAT128N was used for electrochemical measurements and the cell was interfaced with either a photomultiplier tube (PMT, extended-range trialkali S20 PMT, ET Enterprises model 9828B) or charged coupled device (CCD, QEPro, Ocean Optics) for ECL experiments. ECL measurements were conducted in 0.3 M phosphate buffer solution (PBS) with 1, 5 or 10 mM TPrA adjusted to pH 6.8 using NaOH or HCl. Cyclic voltammetry was used to generate the ECL emission with a scan rate of 0.1 V/s. Where ECL was captured using a CCD, an integration time of 500 ms was used (i.e. 50 mV interval spectra were obtained). All experiments were collected in triplicate and signals were averaged. The experimental results are available as open data in public repository [62].

2.3. Numerical simulation

All numerical simulations were executed using the Transport of Diluted Species module in COMSOL Multiphysics v5.5 with a 1D geometry. The reason for this is that the model can be upgraded to more complex 2D geometries in future works, such as those employing ECL with beads or biological cells. The same 1D simulation could also be implemented with more standard packages such as Digielch or Digisim. The model is comprised of three domains at different distances from the electrode surface and with different mesh dimensions (Fig. S2 and Table S3) in order to capture the various chemical reactions operated in the solution: the first 0–20 μm corresponds to the reaction layer in which the homogeneous catalytic processes detailed in Fig. 1 operate, the next 20–50 μm corresponds to the diffusion layer developed during the timescale of the cyclic voltammetry experiment, and finally, the electrolyte (50 μm – 1 cm). Details about reactive species and reactions used in the model along with the kinetic and thermodynamic parameters employed are given in the Supplementary Information (SI).

3. Results and discussion

3.1. Methodology

The primary objective of this work is to find the conditions that, when incorporated in the numerical simulation model, replicate the experimental electrochemical and ECL data for: (i) $[Ru(bpy)_3]^{2+}$/TPrA; (ii) $[Ir^{III}(sppy)_3]^{3-}$/TPrA; and (iii) $[Ir^{III}(sppy)_3]^{3-}$/$[Ru(bpy)_3]^{2+}$/TPrA coreactant systems. Subsequent analysis of these conditions can help rationalize different mechanistic pathways involved in the generation of the ECL signal.

ECL presents the advantage of utilizing two experimental descriptors: (i) electrochemical current potential (i-E) curve that provides insights into the kinetics of major reaction steps, where i is the electrode current and E the electrode potential, and (ii) light emission intensity, I_{ECL}, potential (I_{ECL}-E) curve. Noteworthy, these two descriptors are sensitive to different species or chemical paths (indicated in the SI), which allows a deeper understanding of the whole mechanistic scheme.

In classical ECL experiments where TPrA is used at much higher concentrations than luminophore, the i-E curve is mostly limited by the electrode kinetics of TPrA oxidation. However, the low ECL onset potential in the mixed luminophore coreactant system ($[Ru(bpy)_3]^{2+}$/$[Ir^{III}(sppy)_3]^{3-}$/TPrA) suggests a possible role of $[Ir^{IV}(sppy)_3]^{2-}$ (formed by direct electrooxidation of $[Ir^{III}(sppy)_3]^{3-}$) in the electrocatalytic oxidation of TPrA, followed by its regeneration at the electrode surface (Fig. 1D). This catalytic reaction, with the rate constant k_{fcat}, initiates all homogeneous reactions within the system, effectively altering its reactivity at low anodic overpotentials and as such can be estimated from the electrochemical current. To extract mechanistic information from the current (primarily, to evaluate the efficiency of redox catalysis), we decided to work with lower TPrA concentrations (1 mM, 5 mM and 10 mM) and 1 mM $[Ir^{III}(sppy)_3]^{3-}$. This ensures that both the contributions from direct and mediated TPrA oxidation can be effectively resolved.

However, as the ECL emission of $[Ir^{III}(sppy)_3]^{3-}$ at 515 nm is two orders of magnitude lower than $[Ru(bpy)_3]^{2+}$ (620 nm) [55], a low concentration of $[Ru(bpy)_3]^{2+}$ (500 nM compared to 1 mM $[Ir^{III}(sppy)_3]^{3-}$) needs to be used. In this situation, $[Ru(bpy)_3]^{2+}$ will effectively not contribute to the electrochemistry of the mixed luminophore coreactant system, in which the i-E curve will be equivalent to that of $[Ir^{III}(sppy)_3]^{3-}$/TPrA. Therefore, the mechanistic understanding of the electrochemical (and chemical) steps is obtained by analyzing the TPrA and $[Ir^{III}(sppy)_3]^{3-}$/TPrA systems (Figs. 2 and S3). Conversely, in the mixed luminophore coreactant system, the I_{ECL}-E curve provides insight into the dual $[Ir^{III}(sppy)_3]^{3-}$ and $[Ru(bpy)_3]^{2+}$ ECL emission.

The initial electrochemical characteristics of TPrA and $[Ru(bpy)_3]^{2+}$ are taken from previous simulation works [46,63,64] and changed marginally (for example to account for variations in electrode kinetics

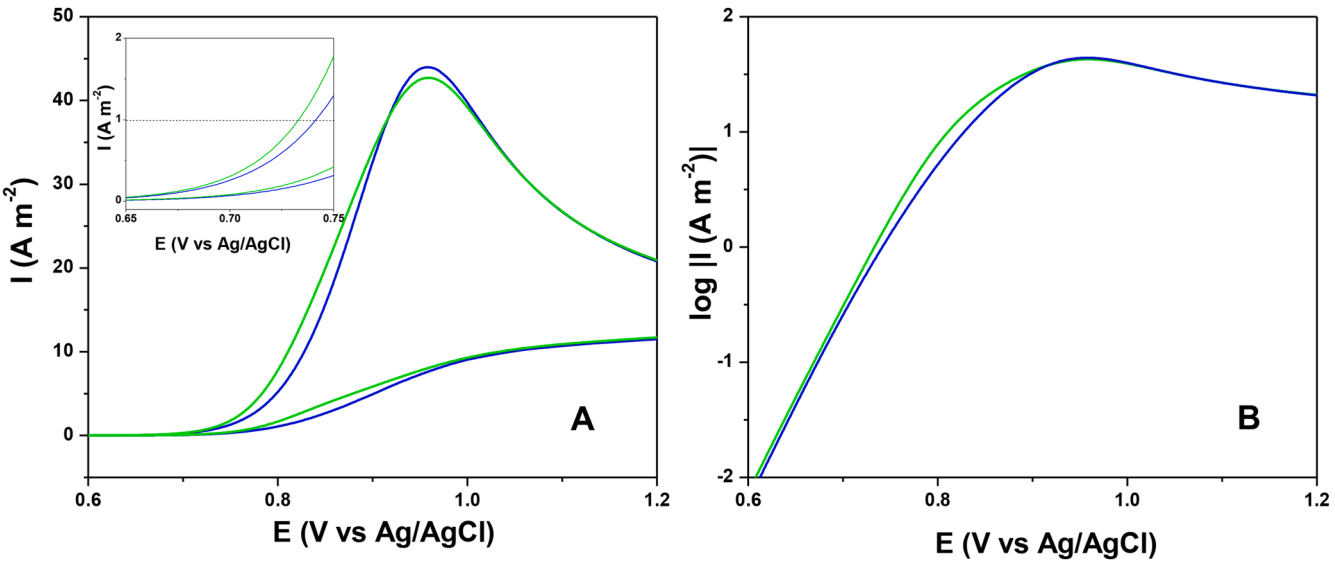

Fig. 2. Simulated **(A)** CVs and **(B)** Tafel plots in 10 mM TPrA solution (blue lines) and 1 mM $[Ir^{III}(sppy)_3]^{3-}$ and 10 mM TPrA solution (green lines). Inset (**A**) shows the magnified foot of the wave region, depicting the difference in onset potentials in 10 mM TPrA solution (blue lines) and 1 mM $[Ir^{III}(sppy)_3]^{3-}$ and 10 mM TPrA solution (green lines).

and to match simulated and experimental data). The electrochemical characteristics of $[Ir^{III}(sppy)_3]^{3-}$ are estimated directly from the experimental results. However, the model, as proposed, implies the involvement of a range of species and reaction steps. It consists of 10, 9 and 14 species participating in 14, 9 and 24 homogeneous plus interfacial steps in the $[Ru(bpy)_3]^{2+}$/TPrA, $[Ir^{III}(sppy)_3]^{3-}$/TPrA and $[Ir^{III}(sppy)_3]^{3-}$/$[Ru(bpy)_3]^{2+}$/TPrA coreactant systems, respectively. The model is, therefore, currently under-characterized, requiring knowledge of numerous parameters or rates. The methodology relies on identifying a minimal set of rate-limiting steps, with other steps considered mass-transfer limited. To do so, we focus on reproducing the experimental curves. The impact of these rate-limited steps on the various i or I_{ECL} responses is then systematically explored.

3.2. *Information extracted from the current*

Cyclic voltammetry (CV) has been successfully used to decipher many homogeneous redox catalysis processes where a redox mediator is used to activate in solution the electrochemistry of molecules, such as H^+, O_2, N_2O, and CO_2, to name a few [59,65–67]. In this respect it should be helpful to decipher ECL mechanisms where a redox mediator is used to activate the oxidation of TPrA, as proposed for the $[Ru(bpy)_3]^{2+}$/$[Ir^{III}(sppy)_3]^{3-}$/TPrA system. Although the electrochemistry of each component of this system has been studied individually, this work seeks to understand their behavior as a whole. We anticipate that the electrochemistry of TPrA will predominantly influence this coreactant system. Nevertheless, comparing the electrochemical behavior of TPrA with that of $[Ir^{III}(sppy)_3]^{3-}$/TPrA, at low concentrations of TPrA, can provide valuable insight into subtle changes in the reactivity of the coreactant system, revealing important mechanistic information.

We performed CV experiments in 0.3 M PBS solutions at pH 6.8 containing 10 mM TPrA, and a mixture of 10 mM TPrA and 1 mM $[Ir^{III}(sppy)_3]^{3-}$ (Figs. S3A and S3D, respectively), and subsequently conducted finite element simulations to replicate the experimental results. The experimental (dashed lines) and the simulated plots (full lines) are in overall agreement, indicating the numerical simulation model can accurately reproduce the experimental data. Minor discrepancies at high potentials can be attributed to convection and/or water oxidation, the effects of which we did not include in the numerical simulation.

Based on the general good agreement, only the simulated i-E plots, shown in Fig. 2, of 10 mM TPrA in the presence (in green) and absence (in blue) of 1 mM $[Ir^{III}(sppy)_3]^{3-}$ are discussed**.** Both CVs have a single irreversible peak corresponding to the oxidation of TPrA, reaching a maximum at approximately 0.95 V. However, in the solution containing $[Ir^{III}(sppy)_3]^{3-}$, the onset of oxidation occurs at a lower overpotential and the CV manifests a shoulder in the current at around 0.80 V vs Ag/AgCl. This potential corresponds to the E^0 of the $[Ir^{III}(sppy)_3]^{3-}$/$[Ir^{IV}(sppy)_3]^{2-}$ redox couple (0.81 V vs Ag/AgCl), determined from experimental and simulated CV plots of 1 mM $[Ir^{III}(sppy)_3]^{3-}$ in the absence of TPrA (Fig. S5). This points to the involvement of the homogeneous catalysis, or activation, of TPrA oxidation (reaction (*1.1*)) by $[Ir(sppy)_3]^{2-}$, the oxidized form of the molecular catalyst $[Ir^{III}(sppy)_3]^{3-}$, electrogenerated at the electrode.

$$\left[Ir(sppy)_3\right]^{2-} + TPrA \rightleftarrows \left[Ir(sppy)_3\right]^{3-} + TPrA^{\bullet+} \quad (1.1)$$

Noteworthy, in such homogeneous molecular catalysis framework [59,60,63–66,68], here employed to catalyze TPrA oxidation, the redox mediator may have a lower standard potential than the TPrA, making the reaction (*1.1*) disfavored or equilibrated and shifted towards reactants reform. However, the deprotonation of the TPrA radical cation following this homogeneous electron transfer step shifts the reaction (*1.1*) to the right and makes it easier at the potential of the redox mediator oxidation. This is detected as an increase in current for the redox mediator oxidation. In fact, the more the homogeneous step is favored (or the faster the deprotonation), the higher the increase in the redox mediator current.

As shown in Figs. 2A and S4A, the difference between the CV responses in the presence and absence of molecular catalysts lies in subtle variations in the foot of the electrochemical waves. To understand the mechanisms at play in this system, it is then important to be able to describe these subtle variations precisely to deduce the contribution of the catalytic reaction. We first used Tafel plots of the CVs constructed by plotting the logarithm of current against the electrode potential. Mechanistic insights are reached from the Tafel plots of the simulated curves of the $[Ir^{III}(sppy)_3]^{3-}$/TPrA system and the TPrA oxidations, shown in Fig. 2B. The shoulder detected in Fig. 2A within the foot of the TPrA oxidation wave is also visible in Fig. 2B: the $[Ir^{III}(sppy)_3]^{3-}$/TPrA system (green line) is characterized by a lower Tafel slope than that of TPrA (blue line). In this potential region, the oxidation of $[Ir^{IV}(sppy)_3]^{2-}$ is probed, which shows faster electrode kinetics than that of TPrA oxidation. At higher overpotentials, a larger Tafel slope is detected as expected for the overlap of both $[Ir^{IV}(sppy)_3]^{2-}$ and TPrA oxidations and

mass transfer control. We therefore analyzed the experimental CV curves through such Tafel plots (Figs. S3B and S3D). While the Tafel slope of TPrA exhibits a value of 86 mV/dec, the Tafel plot of $[Ir^{III}(sppy)_3]^{3-}$/TPrA exhibits a lower slope of 74 mV/dec, confirming that the $[Ir^{III}(sppy)_3]^{3-}$ oxidation occurs before the TPrA oxidation.

Beyond the CV simulation, we utilized foot of the wave analysis (FOWA), a methodology commonly used to benchmark molecular catalysts of electrochemical reactions [60,68], to quantify the catalytic role of $[Ir^{III}(sppy)_3]^{3-}$. FOWA can be expressed by Eq. (1.2) (where i is the current (in A), i_p^0: anodic peak current of the catalyst ($[Ir^{III}(sppy)_3]^{3-}$) in the absence of the substrate (TPrA) (in A), F: the Faraday constant, R: normal gas constant, T: temperature (in K), ν: scan rate (in V/s), E: applied potential (in V), and E°_{Ir}: standard potential of the $[Ir^{III}(sppy)_3]^{3-}/[Ir^{IV}(sppy)_3]^{2-}$ redox couple (in V)). Dividing the catalytic current by i_p^0 circumvents the requirement for independent determination of the electrode surface area, electron transfer kinetics, and the diffusion coefficient to obtain k_{fcat}, the apparent rate constant of the homogeneous redox catalysis reaction (Eq. (1.1)). From Eq. (1.2), the latter rate constant is evaluated from the slope in a FOWA plot where i/i_p^0 is plotted against $1/(1 + \exp(-(F/RT)(E - E_{Ir}^0))$.

$$\frac{i}{i_p^0} = \frac{2.24\sqrt{\frac{RT}{Fv}2k_{fcat}C^0_{TPrA}}}{1+e^{\left(-\frac{F}{RT}\left(E-E^0_{Ir}\right)\right)}} \quad (1.2)$$

The FOWA analysis was performed on the experimental i-E plots for TPrA concentrations of 1, 5 and 10 mM, yielding three different lines (Fig. S6). The slopes of the FOWA lines (2.7, 6.0 and 8.5, respectively) were proportional to the square-root of the TPrA concentration, as expected from Eq. (1.2), yielding a value of k_{fcat} of $2.8 \times 10^3 \pm 0.05 \times 10^3$ $M^{-1}s^{-1}$. This value is then used as an initial guess to simulate the experimental CVs. The value of k_{fcat} for which the best overlap between the simulated and experimental i-E curves is obtained is 3×10^3 $M^{-1}s^{-1}$.

Finally, we tested the relevance of the homogenous catalysis reaction relative to the direct oxidation of TPrA by analyzing the simulated plots of the $[Ir^{III}(sppy)_3]^{3-}$/TPrA in the presence and absence of redox catalysis (k_{fcat} = to 3×10^3 $M^{-1}s^{-1}$ and $k_{fcat} = 0$ $M^{-1}s^{-1}$, respectively). This discussion is detailed in the SI using Figs. S6 and S7, from which it is concluded that the primary contribution of $[Ir^{III}(sppy)_3]^{3-}$ to the electrochemical current, at low potentials, arises from the homogeneous catalysis of TPrA.

On a more general note, considering the complexity of the chemical and electrochemical processes involved, various combinations of thermodynamic and kinetic parameters could lead to a satisfactory alignment between the simulated and experimental results. Specifically, factors such as the rate of $TPrAH^+$ deprotonation, oxidation potentials of TPrA and $[Ir^{III}(sppy)_3]^{3-}$ and the rate constants of the corresponding electron transfer steps, deprotonation of $TPrA^{\bullet+}$, rates of homogeneous catalysis and the reaction between the oxidized $[Ir^{IV}(sppy)_3]^{2-}$ and $TPrA^{\bullet}$, which populates the $[Ir^{III}(sppy)_3]^{3-*}$ excited state can all have a profound influence on the shape of the i-E curves in the mixed luminophore coreactant system. However, previous experimental [69,70] and numerical simulation [46,63,64] studies have contributed to determining some of these parameters, reducing uncertainty in our model predictions of the current.

3.3. ECL of $[Ru(bpy)_3]^{2+}$/TPrA coreactant system

ECL is inherently bound to the homogeneous reactivity of the most reactive transient species, namely the $TPrA^{\bullet}$ radical (as seen in Fig. 1). The ECL light emission then provides a complementary sensitive output that can help decipher further the activity of such transient species in the vicinity of the electrode surface. To gain mechanistic insights, we captured ECL spectra in the range from 350 nm to 1150 nm over a CV scan from 0.1 V to 1.5 V (Fig. S9). This approach allowed us to analyze the evolution of ECL intensity with electrochemical potential, while distinguishing the contributions of $[Ir^{III}(sppy)_3]^{3-}$ and $[Ru(bpy)_3]^{2+}$ to the total light emission based on their distinct emission wavelengths (515 nm and 620 nm, respectively).

Fig. 3 shows the simulated (full line) and experimental (dashed line) ECL intensity-potential plots at 620 nm, namely $I_{ECL,Ru}$-E, for the 500 nM $[Ru(bpy)_3]^{2+}$ and 10 mM TPrA solution in 0.3 M PBS pH 6.8. To simulate the $I_{ECL,Ru}$-E plot, we integrated all photons that correspond to the emission of $[Ru(bpy)_3]^{2+}$ over the whole volume of solution (at all distances from the electrode surface) and plotted the integrated values against the electrochemical potential. The simulated $I_{ECL,Ru}$ increases with potential in a sigmoidal fashion, with the half wave potential at around 1.08 V vs Ag/AgCl (0.22 V higher than the half wave potential of TPrA oxidation, see Fig. 2) and reaching the maximum at approximately 1.2 V. The ECL emission at low anodic overpotentials is a result of the heterogeneous ("remote") pathway (Fig. 1A). However, at potentials above the E^0 of the $[Ru(bpy)_3]^{2+}/[Ru(bpy)_3]^{3+}$ redox couple (1.04 V vs Ag/AgCl), the mechanistic route including direct oxidation of $[Ru(bpy)_3]^{2+}$ prevails, controlling the steady-state emission. To demonstrate this contribution, we plotted the evolution of the concentrations of TPrA, $[Ru(bpy)_3]^{2+}$, and $[Ru(bpy)_3]^{3+}$ species at the electrode surface with potential (Fig. S10). All three concentration-potential profiles are sigmoidal, with half-wave potentials of 0.91 V, 1.10 V and 1.10 V, respectively. The half-wave potential of the $I_{ECL,Ru}$-E plot is 1.08 V, indicating the reliance of ECL emission on the generation of $[Ru(bpy)_3]^{3+}$ species at the electrode surface.

The described simulated plot (full line) in Fig. 3 is in agreement with the experimental one (dashed line) within the activation regime (in which $I_{ECL,Ru}$ increases with the potential). However, while the simulation predicts a steady state behavior, the experimental plot exhibits a distinct peak at 1.2 V and ECL depletion at higher potentials. The sigmoidal shape of this ECL signal loss with the electrode potential suggests a potential-induced quenching of the ECL (with the formal potential $E^0_{app,qECL} = 1.32$ V vs Ag/AgCl). This can be attributed to the electrode surface oxidation influencing electron transfer rates and affecting the $TPrA^{+\bullet}$ deprotonation constant, causing depletion of the TPrA radicals [71–73]. As previously discussed, the oxidation of TPrA involves a proton-coupled electron transfer, initially yielding a radical cation intermediate that rapidly deprotonates forming a neutral radical. The concentration ratio of these radical species determines the dominant ECL pathway, shaping the resulting emission. However, anodically polarized GCE can undergo surface oxidation, and the formed oxygen-containing functional groups can serve as proton acceptors, facilitating the deprotonation of $TPrA^{\bullet+}$. Consequently, $TPrA^{\bullet}$ radicals form closer to the electrode surface, where they are scavenged before participating in the ECL reactions. Therefore, a decreased lifetime of $TPrA^{\bullet+}$ diminishes the concentration of both TPrA radicals, decreasing

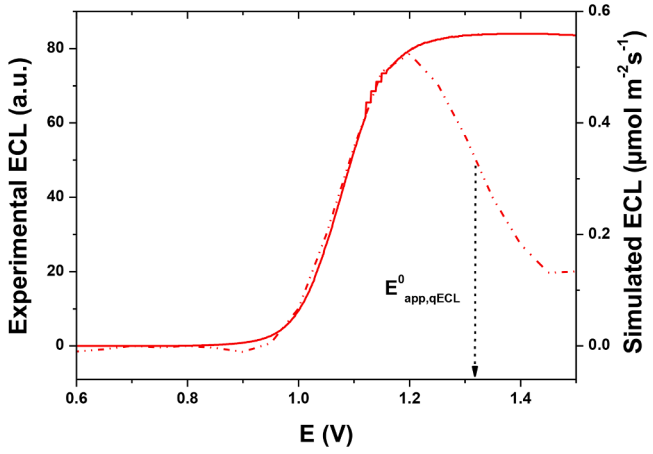

Fig. 3. Simulated (full line) and experimental (dashed line) ECL intensity at 620 nm in 500 nM $[Ru(bpy)_3]^{2+}$ and 10 mM TPrA solution.

the efficiency of the coreactant ECL pathways and leading to ECL quenching. Other possible reasons are the formation of undesired oxidation products, and ECL quenching by electrogenerated species. Given the complexity of these processes, we did not consider them in the numerical simulation and will not further discuss them.

3.4. ECL of $[Ir^{III}(sppy)_3]^{3-}$/TPrA coreactant system

The unique redox properties of $[Ir^{III}(sppy)_3]^{3-}$, distinct from those of $[Ru(bpy)_3]^{2+}$, play a pivotal role in the ECL behavior of this coreactant system. Specifically, the oxidation potential of $[Ir^{III}(sppy)_3]^{3-}$ ($E^0_{Ir(IV),Ir(III)}$ = 0.81 V) is slightly lower than that of TPrA (E^0_{TPrA} = 0.96 V), enabling its direct electrooxidation followed by the homogenous electron transfer producing TPrA radicals (catalytic route, Fig. 1D). As demonstrated in previous sections, this reaction facilitates all (electro) chemical steps at low anodic potentials, leading to a low ECL onset potential. Moreover, the low reduction potential of this redox mediator (ca. −2.0 V) prevents its reduction by $TPrA^{\bullet}$, limiting $[Ir^{III}(sppy)_3]^{3-}$ ECL generation to only one possible route (Fig. 1B). Therefore, before exploring ECL in the mixed luminophore system, it is imperative to construct a model that accurately replicates the properties of the $[Ir^{III}(sppy)_3]^{3-}$/TPrA coreactant system.

We recorded ECL spectra of the solutions containing 1 mM $[Ir^{III}(sppy)_3]^{3-}$ with 1 mM, 5 mM and 10 mM TPrA in 0.1 M PBS pH 7.4. Fig. 4 presents the experimental ECL intensity potential, $I_{ECL,Ir}$-E, plots constructed from the spectroscopic ECL evolution recorded at 515 nm. Subsequently, we employed numerical simulations, starting from the homogeneous catalysis scheme devised above (Fig. 1D), to reproduce the experimental results, Fig. 4 (solid lines). It shows that the simulated data follow the general trend observed in the experimental results. Although the CV responses match well (Fig. S3C), the alignment is lower for the ECL responses (Fig. 4) (less than what was seen in the case of the $[Ru(bpy)_3]^{2+}$ ECL in Fig. 3). Notably, the experimental ECL onset occurs at low anodic potential values, with a half wave potential at 0.81 V vs Ag/AgCl (which corresponds to the E^0 of the $[Ir^{III}(sppy)_3]^{3-}$/$[Ir^{IV}(sppy)_3]^{2-}$ redox couple) for all three $[Ir^{III}(sppy)_3]^{3-}$: TPrA concentration ratios, indicating that excited state production requires the oxidation of $[Ir^{III}(sppy)_3]^{3-}$ at the electrode. If the oxidation–reduction route (Fig. 1B) can be postulated, the $TPrA^{\bullet}$ (necessary to populate the excited state) needs to be generated efficiently at low anodic overpotentials compared to the direct heterogeneous oxidation of TPrA, providing further evidence for TPrA oxidation via the homogeneous catalytic mechanism (Fig. 1D).

However, while the ECL intensity, $I_{ECL,Ir}$, increases with the increase in TPrA concentration, this relationship is not linear, suggesting that one of the species involved in the electrochemical oxidation of TPrA is quenching the $[Ir^{III}(sppy)_3]^{3-}$ ECL. As a first possible explanation, it might be due to oxidative quenching of $[Ir^{III}(sppy)_3]^{3-*}$ excited state by $TPrA^{\bullet+}$ (reaction (*2.1*)), as previously reported for the related $Ir^{III}(ppy)_3$ complex [74]. Indeed, taking into account such reaction into the model can reproduce the general experimental trends (simulated data in Fig. 4A). However, to be operative, the rate constant for this reaction needs to be set at $k_{fq} = 10^{12}\ M^{-1}s^{-1}$, a rate exceeding the bimolecular diffusion limit. As a reference, the simulated plots in Fig. S11A illustrate the difference in ECL under the abovementioned conditions with quenching reaction rate constants of $10^{12}\ M^{-1}s^{-1}$ (full lines) and diffusion-limited value of $10^{10}\ M^{-1}s^{-1}$ (dotted lines).

$$\left[Ir(sppy)_3\right]^{3-*} + TPrA^{\bullet+} \xrightarrow{k_{fq}} \left[Ir(sppy)_3\right]^{2-} + TPrA \qquad (2.1)$$

The practically unattainable rate of the oxidative quenching reaction that was necessary to replicate the experimental results indicates it is not the only process that affects the intensity of ECL emission at 515 nm. One possible explanation is that the reaction producing the excited state of $[Ir^{III}(sppy)_3]^{3-*}$ (reaction (*2.2*), rate constant k_{f6}), initiated by the oxidation of the $TPrA^{\bullet}$ radical, is rate-limiting rather than diffusion-limited. This limitation may be due to the comparable values of the $TPrA^{\bullet}$ oxidation potential (ca. −1.7 V) to that of the $[Ir^{IV}(sppy)_3]^{2-}$/$[Ir^{III}(sppy)_3]^{3-*}$ couple: $E^0_{IV/III*} = E^0_{IV/III} - E_{em,Ir}$ = 0.8 – 2.4 = −1.6 V (where $E_{em,Ir}$ is the energy associated to photon emission at 515 nm). If this is true, other reactions, especially redox catalysis, could deplete $[Ir^{IV}(sppy)_3]^{2-}$ species, further decelerating the rate of $[Ir^{III}(sppy)_3]^{3-*}$ excited state formation and limiting the maximum ECL output, affecting the efficiency of this ECL coreactant system. This kinetic control of ECL emission becomes more evident at higher concentrations of TPrA, where the rate of homogeneous catalysis increases, leading to behavior resembling quenching.

$$\left[Ir(sppy)_3\right]^{2-} + TPrA^{\bullet} \xrightarrow{k_{f6}} \left[Ir(sppy)_3\right]^{3-*} + P \qquad (2.2)$$

The role of such reaction on $I_{ECL,Ir}$ was also tested through simulation. $I_{ECL,Ir}$-E plots in Fig. 4B were simulated without taking the oxidative quenching into account (reaction (*2.1*); $k_{fq} = 0\ M^{-1}s^{-1}$), and considering kinetically-limited reaction (*2.2*) in the numerical simulation model. The best fit obtained in Fig. 4B is reached for the reaction rate constant of $k_{f6} = 8 \times 10^7\ M^{-1}s^{-1}$. The intensities of as obtained $I_{ECL,Ir}$-E plots (in full lines) are in agreement with the experimentally

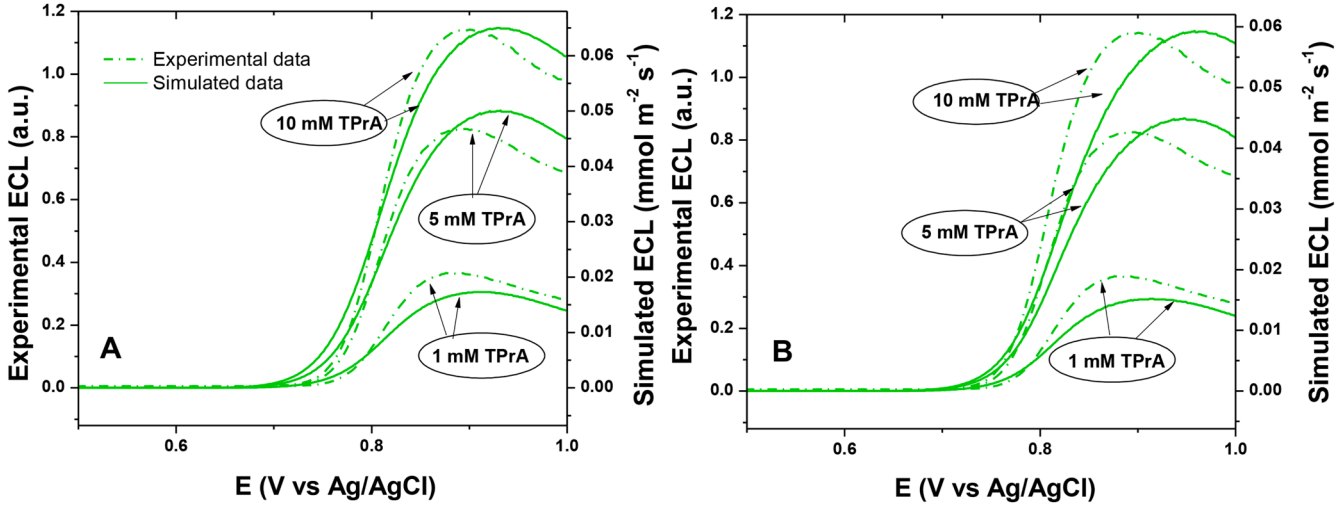

Fig. 4. Simulated ECL intensities (full lines) and experimental ECL intensities (dashed lines) at 515 nm for 1 mM $[Ir^{III}(sppy)_3]^{3-}$ and 1 mM, 5 mM, and 10 mM TPrA solutions. Simulated plots are estimated from the model that **(A)** included the oxidative quenching reaction (*2.1*), with a rate of $k_{fq} = 10^{12}\ M^{-1}s^{-1}$ and a rate constant of $[Ir^{III}(sppy)_3]^{3-*}$ excited state production, reaction (*2.2*), $k_{f6} = 10^9\ M^{-1}s^{-1}$ and **(B)** did not include the oxidative quenching and $k_{f6} = 8 \times 10^7\ M^{-1}s^{-1}$.

obtained maximal ECL intensities (dotted lines), supporting the role of kinetic control over the ECL emission. Noteworthy, as shown in Fig. S11B, for higher k_{f6} values, the $I_{ECL,Ir}$ yields poorer fit as it becomes proportional to the TPrA concentration.

Fig. 4 demonstrates the borderline cases where the non-linear correlation between the ECL intensity response and TPrA concentration is explained either by oxidative quenching of $[Ir^{III}(sppy)_3]^{3-*}$ excited state by $TPrA^{\bullet+}$ or by the kinetically slow generation of the excited state. In reality, both effects may contribute to this suboptimal ECL output of $[Ir^{III}(sppy)_3]^{3-}$/TPrA coreactant system. More generally, Fig. 4 illustrates how this suboptimal ECL output is bound to electron transfer steps between the $[Ir^{IV}(sppy)_3]^{2-}/[Ir^{III}(sppy)_3]^{3-*}$ redox couple with TPrA-related species. Different combinations of the abovementioned reaction rates could provide simulated plots that resemble the experimental ones, and there is no way to estimate the absolute values of all the rate constants without further experimental proof. Nevertheless, the numerical simulation model provides the means to study the mutual dependence of reaction steps, giving insight into their contribution to the electrochemical and ECL behavior of this coreactant system.

Lastly, Fig. 4 shows a mismatch between the evolution of simulated and experimental ECL intensity with potential. The shift in ECL peak to higher potential values is evident in both Fig. 4A and 4B. This discrepancy is more pronounced in Fig. 4B, where the half-wave potential for the simulated curves equals 0.83 V. Conversely, the half-wave potential in Fig. 4A matches the experimental one (of 0.81 V), but the ECL onset is shifted to lower overpotentials. This observation suggests that the rate of $[Ir^{III}(sppy)_3]^{3-*}$ excited state generation will influence not only the intensity but also the onset potential of ECL emission. This effect is indirect and involves the interplay of reaction (*2.2*) with other chemical and electrochemical steps, which will be discussed in the following sections.

3.5. Simulating ECL to study reactivity in the mixed $[Ir^{III}(sppy)_3]^{3-}/[Ru(bpy)_3]^{2+}$/TPrA system

While systematic study of $[Ru(bpy)_3]^{2+}$/TPrA and $[Ir^{III}(sppy)_3]^{3-}$/TPrA provided insight into the mechanistic schemes of both coreactant ECL systems, to comprehend the reactivity of the $[Ir^{III}(sppy)_3]^{3-}/[Ru(bpy)_3]^{2+}$/TPrA system in its entirety, we recognize the need to consider it holistically. Despite its inherent complexity, involving numerous reaction species and steps, constructing a numerical simulation model that encompasses the complete reactivity of the mixed luminophore/coreactant system is feasible. This arises from the possibility of defining the model (or rather reducing the number of unknown variables) by incorporating information obtained during the preliminary analysis of the $[Ru(bpy)_3]^{2+}$/TPrA and $[Ir^{III}(sppy)_3]^{3-}$/TPrA systems, and further refining it by comparing the simulated data with the experimental ECL plots. This strategy allows for discerning the rate-limiting reactions in the system. By discussing the influence of the rates of these reactions on the simulated i-E and I_{ECL}-E plots, we can gain insight that serves both a predictive purpose, if one is able to synthesize other co-redox mediators, and an exploratory one, revealing the intricate interplay between different mechanistic steps.

Fig. S12A shows simulated CV plots of the mixed luminophore coreactant system upon systematically increasing the rate of $[Ir^{III}(sppy)_3]^{3-*}$ excited state generation. Interestingly, this rate also affects the electrochemical curve, and an increase in k_{f6} leads to a decrease in the peak potentials, seemingly leading to the increase in the rate of electrochemical oxidation of TPrA. This effect can be rationalized by the influence of the rate of reaction (*2.2*) on the deprotonation of $TPrA^{\bullet+}$ (reaction (*3.1*), rate constant $k_{f0} = 10^4\ s^{-1}$). The higher the rate k_{f6}, the faster the consumption of $TPrA^{\bullet}$ (reaction (*2.2*)), which shifts the equilibrium of $TPrA^{\bullet+}$ deprotonation (Eq. (3.2)) to the right. This, in turn, accelerates the rate of TPrA oxidation (Eq. (3.1)), either from the electrode (direct oxidation) or from the redox catalysis routes, affecting the current response.

$$TPrA \rightarrow e^- + TPrA^{\bullet+} \tag{3.1}$$

$$TPrA^{\bullet+} \rightleftarrows TPrA^{\bullet} + H^+ \tag{3.2}$$

This rate has even stronger effect on the ECL generation than on the electrode current. Fig. S12B shows the ECL intensity at 515 nm (attributed to $[Ir^{III}(sppy)_3]^{3-}$) increasing with a higher rate constant of $[Ir^{III}(sppy)_3]^{3-*}$ generation. Additionally, the ECL onset potential shifts to lower values with the increase in the k_{f6}, indicating that apart from directly increasing the rate of $[Ir^{III}(sppy)_3]^{3-*}$ formation, an increase in k_{f6} accelerates the formation $TPrA^{\bullet}$ (through reactions (*3.1*) and (*3.2*) under the direct and the redox catalytic routes) that is necessary to populate the luminophore's excited state, consequently triggering the ECL emission at low anodic overpotentials.

In contrast, the ECL intensity at 620 nm ($[Ru(bpy)_3]^{2+}$ emission) decreases with the increase in the rate of reaction (*2.2*) and $I_{ECL,Ru}$ onset shifts to higher potentials (Fig. S12C). The reason for this can be the depletion of the pool of TPrA radicals at high rates of k_{f6}. Since both $TPrA^{\bullet+}$ and $TPrA^{\bullet}$ are necessary for populating the $[Ru(bpy)_3]^{2+*}$ excited state (Eqs. (4.1), (4.2) and (4.3)), the ECL emission of $[Ru(bpy)_3]^{2+}$ is controlled by the rate of their consumption in reactions (*2.2*) and (*3.2*).

$$[Ru(bpy)_3]^{2+} + TPrA^{\bullet} \rightarrow [Ru(bpy)_3]^{+} + P \tag{4.1}$$

$$[Ru(bpy)_3]^{+} + TPrA^{\bullet+} \rightarrow [Ru(bpy)_3]^{2+*} + TPrA \tag{4.2}$$

$$[Ru(bpy)_3]^{3+} + TPrA^{\bullet} \rightarrow [Ru(bpy)_3]^{2+*} + P \tag{4.3}$$

This demonstrates how, although reaction (*2.2*) initially appears to affect only the intensity of $[Ir^{III}(sppy)_3]^{3-}$ ECL emission, its interplay with other reactions profoundly shapes the reactivity of the entire mixed luminophore coreactant system.

However, this was only explored here in the situation where the homogeneous reduction of $[Ir^{III}(sppy)_3]^{3-}$ by $TPrA^{\bullet}$ (reaction (*5.1*)) was neglected, due to its thermodynamic unfavourability, since the redox potential of the $TPrA^{\bullet}/P$ redox couple (−1.6 V vs Ag/AgCl) is more positive than that of $[Ir^{II}(sppy)_3]^{4-}/[Ir^{III}(sppy)_3]^{3-}$ (−2.0 V vs Ag/AgCl), making this reduction reaction unlikely. Noteworthy the reduced form of the $[Ir^{III}(sppy)_3]^{3-}$ is denoted $[Ir^{II}(sppy)_3]^{4-}$ even though formally the electron is borne by the ligand rather than the metal center.

$$[Ir(sppy)_3]^{3-} + TPrA^{\bullet} \rightarrow [Ir(sppy)_3]^{4-} + P \tag{5.1}$$

$$[Ir(sppy)_3]^{4-} + TPrA^{\bullet+} \rightarrow [Ir(sppy)_3]^{3-*} + TPrA \tag{5.2}$$

$$[Ir(sppy)_3]^{4-} + [Ir(sppy)_3]^{2-} \rightarrow [Ir(sppy)_3]^{3-*} + [Ir(sppy)_3]^{3-} \tag{5.3}$$

Nevertheless, its impact on this coreactant system should not be completely disregarded as it can serve for predictive purposes, for example when iridium complexes with different ligand structures are employed [40,57,75–77]. A newly introduced set of reactions is then taken into account. Simulations incorporating these reactions provide insights into the anticipated I_{ECL}-E behaviors. Reaction (*5.1*) would not only deplete $TPrA^{\bullet}$, thus lowering the rate of reaction (*2.2*), but it would also open alternative routes for populating $[Ir^{III}(sppy)_3]^{3-*}$ excited state (Eqs. (5.2) and (5.3)). Overall, this set of reactions decreases the influence of k_{f6} rate constant on the ECL of the Ir species, $I_{ECL,Ir}$.

It further affects the overall ECL in the mixed luminophore coreactant system, and therefore the emission of photons from the Ru species, $I_{ECL,Ru}$. If reaction (*5.1*) proceeds at high rates, it depletes the pool of $TPrA^{\bullet}$ and localizes them near the electrode surface (Fig. S13A), consequently confining the emission layer of $[Ru(bpy)_3]^{2+}$ ECL (Fig. S13B). Furthermore, with an increase in the rate of reaction (*5.1*), the intensity of $[Ru(bpy)_3]^{2+}$ emission decreases and the ECL onset shifts to higher potentials (Fig. S14). This behavior once again

demonstrates the control of $[Ru(bpy)_3]^{2+}$ ECL emission by the concentration of $TPrA^{\bullet}$ (Eqs. (4.1), (4.2) and (4.3)). The role of the Ir redox catalyst allows fine-tuning of the potential and spatial distribution of the reactive intermediates $TPrA^{\bullet}$ and $TPrA^{+\bullet}$ and consequently the ECL emissions.

The simulation results indicate that in reaction (*5.1*), $TPrA^{\bullet}$ is consumed, affecting the ECL signal by artificially shortening this radical's lifetime. Despite TPrA serving as a sacrificial coreactant in various ECL systems, the lifetime of its neutral radical is unknown. Thus, the numerical simulation treats $TPrA^{\bullet}$ as a long-lived species, propagating here up to 30 μm (Fig. S13A), potentially introducing inaccuracies in the predicted ECL behavior of the system. Given that this highly reactive radical plays a pivotal role in governing ECL reactions and its spatial expansion, it becomes crucial to experimentally determine its stability. For example, based on the predicted spatial light emission profile in Fig. S13B, analyzing the spatial distribution of ECL emission layer, as proposed by Su and co-workers' [49,78], in such a mixed system could help quantify the $TPrA^{\bullet}$ stability. This knowledge not only advances our comprehension of the mixed luminophore ECL system but also contributes to a broader understanding of all coreactant systems involving TPrA or other tri-substituted amines.

While the reaction steps discussed so far provide valuable information on the mutual influence of interconnected mechanistic routes and the way their interplay shapes the ECL of the investigated coreactant system, we cannot obtain unambiguous information about their influence on the ECL without further complementary experimental evidence. In this context, one must not forget the main aim of this study, which is to comprehend the intricate influence of the incorporation of $[Ir^{III}(sppy)_3]^{3-}$ in the $[Ru(bpy)_3]^{2+}$/TPrA coreactant system has on the $[Ru(bpy)_3]^{2+}$ ECL emission at 620 nm. We initially postulated that the two mechanistic steps responsible for the earlier onset potential and enhanced $[Ru(bpy)_3]^{2+}$ ECL intensity at low anodic overpotentials are the inter-catalyst electron transfer exchange leading to the redox-mediated oxidation of $[Ru(bpy)_3]^{+}$ (reaction (*6.1*), rate constant $k_{f,IrRu}$), and the homogeneous catalysis of TPrA oxidation (k_{fcat}, reaction (*1.1*)). Therefore, in the final, exploratory part of this study, we simulated the $[Ru(bpy)_3]^{2+}$ ECL emission at 620 nm, $I_{ECL,Ru}$, while systematically varying the rate constants of these reactions (Fig. 5). In an effort to simplify the numerical simulation model, and to adapt to the structure of the present Ir complex, the homogeneous reduction of $[Ir^{III}(sppy)_3]^{3-}$ (reaction (*5.1*)) will be neglected in all further considerations.

$$[Ru(bpy)_3]^{+} + [Ir(sppy)_3]^{2-} \rightarrow [Ru(bpy)_3]^{2+*} + [Ir(sppy)_3]^{3-} \quad (6.1)$$

Fig. 5A depicts simulated $I_{ECL,Ru}$-E plots at 620 nm showing the influence of the kinetics of reaction (*6.1*). As $k_{f,IrRu}$ increases, the ECL shifts to lower potentials ($I_{ECL,Ru}$ peak transitions from 1.2 V at $k_{f,IrRu} = 10^4\ M^{-1}s^{-1}$ to 0.90 V at $k_{f,IrRu} = 3 \times 10^6\ M^{-1}s^{-1}$), accompanied by an elevation in emission intensity. This trend indicates that the introduction of an alternative pathway for $[Ru(bpy)_3]^{+}$ oxidation enhances the efficiency of $[Ru(bpy)_3]^{2+*}$ excited state generation, consequently amplifying the $[Ru(bpy)_3]^{2+}$ ECL intensity. The high efficiency of reaction (*6.1*) is rationalized by its driving force of −0.16 V owing to the difference between the E^0 values of the $[Ir^{III}(sppy)_3]^{3-}/[Ir^{IV}(sppy)_3]^{2-}$ and $[Ru(bpy)_3]^{+}/[Ru(bpy)_3]^{2+*}$ redox couples (0.81 V and 0.65 V vs Ag/AgCl, respectively). The potential of the $[Ru(bpy)_3]^{+}/[Ru(bpy)_3]^{2+*}$ redox couple is calculated as: $E^0_{+/2+*} = E^0_{+/2+} + E_{em,Ru}$ (where $E_{em,Ru} = 2$ eV is the energy associated to photon emission at 620 nm). Additionally, the emergence of ECL emission at a lower potential, where only $[Ir(sppy)_3]^{3-}$ can be directly oxidized at the electrode (see Fig. 6A), suggests $TPrA^{\bullet}$ is produced in this potential region, which then generates $[Ru(bpy)_3]^{+}$. This strongly supports the homogeneous oxidation of TPrA by $[Ir^{III}(sppy)_3]^{3-}$ through reaction (*1.1*) (Fig. 1D). Moreover, in the absence of the inter-catalyst electron exchange (reaction (*6.1*), Fig. 1C), the extent of $[Ru(bpy)_3]^{2+}$ ECL would rely only on the availability of $TPrA^{\bullet}$ and $TPrA^{\bullet+}$, with the luminophores operating independently. The oxidized form of the iridium complex being produced at the electrode, the homogeneous electrocatalysis of TPrA is expected to produce both $TPrA^{\bullet+}$ and $TPrA^{\bullet}$ within the first few micrometers from the electrode. This enable the generation of $[Ru(bpy)_3]^{+}$ and then ECL emission depending on the efficiency of the inter-catalyst exchange rate and of the homogeneous electrocatalysis. On the one hand, the lower the inter-catalyst exchange rate the lower the $[Ru(bpy)_3]^{2+}$ ECL and the more it is shifted towards more positive potential as confirmed from the trend in Fig. 5A.

Therefore, as previously discussed and confirmed here by simulation, in the presence of $[Ir^{III}(sppy)_3]^{3-}$, the $[Ru(bpy)_3]^{2+}$ ECL onset potential observed within the Ir complex oxidation potential region, demonstrates the significant contribution of the redox-mediated route (Fig. 1C) to the overall mechanistic scheme.

As just mentioned, the $[Ru(bpy)_3]^{2+}$ ECL at low potential in the mixed luminophore ECL system also requires the homogeneous oxidation of TPrA by $[Ir^{IV}(sppy)_3]^{2-}$ (reaction (*1.1*), rate constant k_{fcat}); we therefore investigated its influence on the dual ECL emission. We

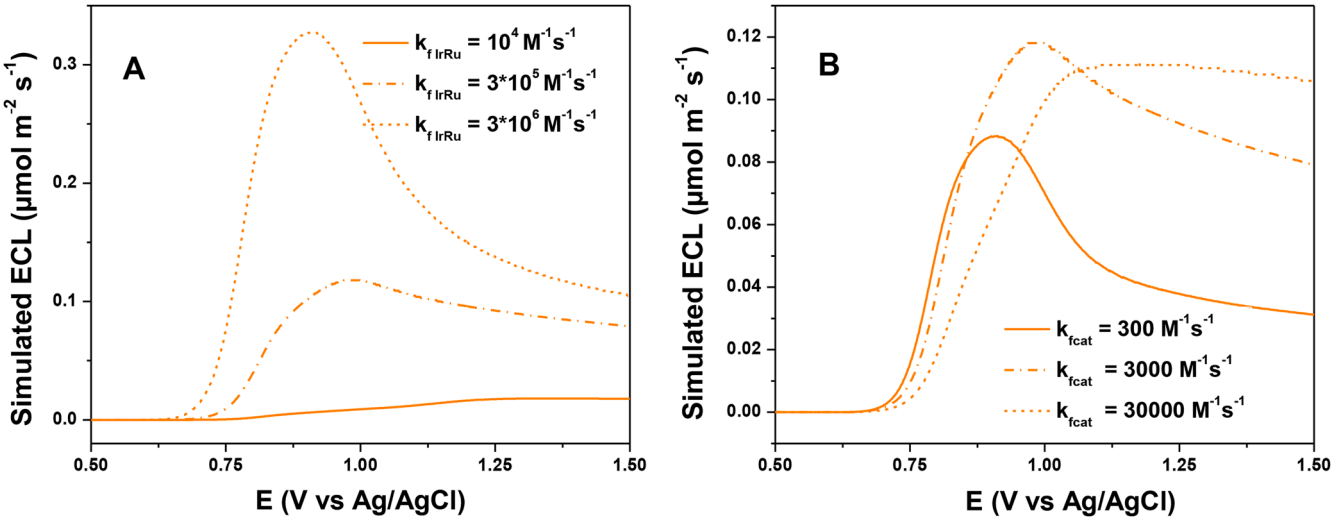

Fig. 5. Simulated $[Ru(bpy)_3]^{2+}$ ECL intensities at 620 nm, $I_{ECL,Ru}$, in 1 mM $[Ir^{III}(sppy)_3]^{3-}$, 500 nM $[Ru(bpy)_3]^{2+}$ and 10 mM TPrA solution with **(A)** the inter-Ir-Ru species 'redox-mediated' step rate $k_{f,IrRu}$ is $10^4\ M^{-1}s^{-1}$ (full line), $3 \times 10^5\ M^{-1}s^{-1}$ (dashed line) and $3 \times 10^6\ M^{-1}s^{-1}$ (dotted line) when k_{fcat} is set to $3 \times 10^3\ M^{-1}s^{-1}$; and **(B)** the rate of redox catalysis $3 \times 10^2\ M^{-1}s^{-1}$ (full line), $3 \times 10^3\ M^{-1}s^{-1}$ (dashed line) and $3 \times 10^4\ M^{-1}s^{-1}$ (dotted line) when $k_{f,IrRu} = 3 \times 10^5\ M^{-1}s^{-1}$.

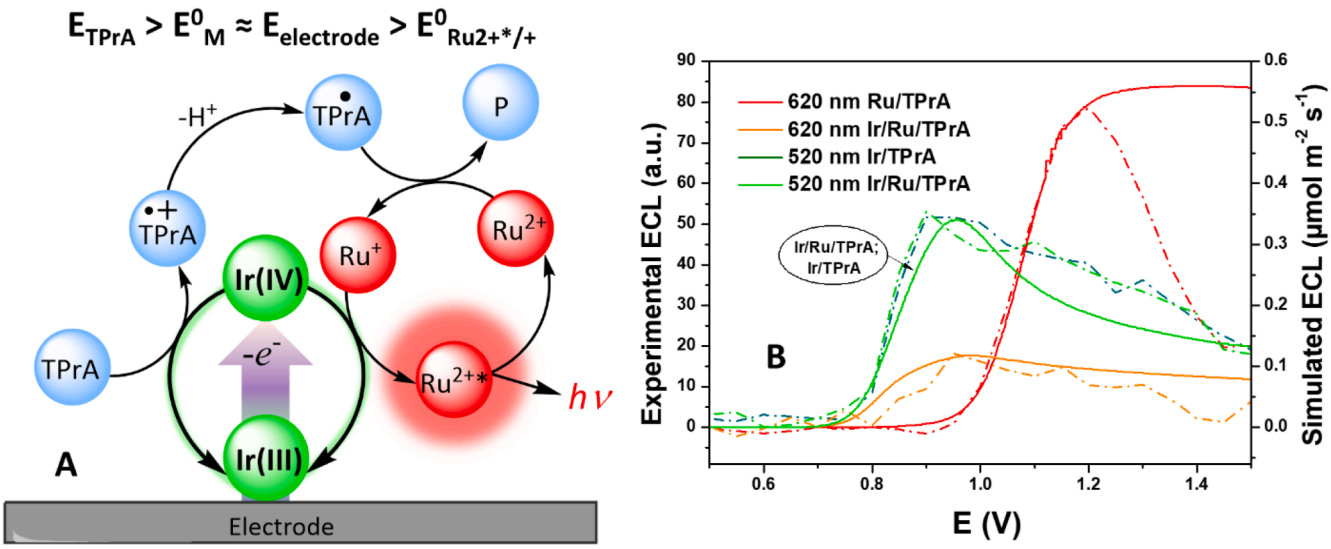

Fig. 6. **(A)** Schematic illustrating the role of the Ir(III) electrocatalyst in the oxidation of TPrA and Ru(I) species, leading to amplified $[Ru(bpy)_3]^{2+}$ ECL at low anodic potentials. **(B)** Simulated (full lines) and experimental (dashed lines) ECL intensities: at 620 nm in 500 nM $[Ru(bpy)_3]^{2+}$ and 10 mM TPrA solution (red lines); at 620 nm in 1 mM $[Ir^{III}(sppy)_3]^{3-}$, 500 nM $[Ru(bpy)_3]^{2+}$ and 10 mM TPrA solution (orange lines); at 515 nm in 1 mM $[Ir^{III}(sppy)_3]^{3-}$and 10 mM TPrA solution (green lines); and at 515 nm in 1 mM $[Ir^{III}(sppy)_3]^{3-}$, 500 nM $[Ru(bpy)_3]^{2+}$ and 10 mM TPrA solution (cyan lines).

previously estimated the k_{fcat} from the electrochemical currents, the i-E plots ($k_{fcat} = 3 \times 10^3\ M^{-1}s^{-1}$), but a more in-depth analysis would improve our understanding of the overall reactivity within this co-reactant system. Moreover, analyzing the ECL behavior at different rates of redox catalysis can serve a predictive purpose, if one can synthesize other redox mediators.

Fig. 5B illustrates simulated $I_{ECL,Ru}$-E plots at 620 nm with varying k_{fcat} values. As k_{fcat} increases, the ECL onset potential becomes more positive. Notably, the plots exhibit a shoulder at low overpotentials, in the $[Ir^{III}(sppy)_3]^{3-}$ oxidation region, attesting the role of the $[Ir^{III}(sppy)_3]^{3-}$/TPrA redox catalysis on the $[Ru(bpy)_3]^{2+}$ ECL. At higher potentials, for lower k_{fcat} values ($3 \times 10^2\ M^{-1}s^{-1}$ and $3 \times 10^3\ M^{-1}s^{-1}$), the $I_{ECL,Ru}$-E plots show peaks (maximum of $I_{ECL,Ru}$), while it is transitioning to a steady-state behavior at higher rate constant values (above $3 \times 10^4\ M^{-1}s^{-1}$). Furthermore, the faster the k_{fcat}, the higher the peak ECL intensity, reaching its highest value for k_{fcat} close to $3 \times 10^3\ M^{-1}s^{-1}$ and decreasing at higher rate constants (where ECL is characterized by steady-state emission).

Reaction (*1.1*) controls the ECL intensity by controlling the production of $TPrA^{\bullet+}$ (and $TPrA^{\bullet}$ through reaction (*3.2*)), which is responsible for the population of the $[Ru(bpy)_3]^{2+*}$ excited state (Eqs. (4.1), (4.2) and (4.3)). Simultaneously, $[Ir^{IV}(sppy)_3]^{2-}$ species are depleted during this reaction. At low concentrations of $[Ir^{IV}(sppy)_3]^{2-}$ the rate of redox-mediated $[Ru(bpy)_3]^{+}$ oxidation (reaction *6.1*) decreases, becoming comparable to the one governed by $TPrA^{\bullet+}$ (reaction (*4.2*)). These competing reactions impose as steady-state (potential independent) of the concentration of the $[Ru(bpy)_3]^{2+*}$ species. Consequently, the faster k_{fcat} rates cause a transition from the ECL emission controlled by the redox-mediated route (Fig. 1C) to the one controlled by the remote route (Fig. 1A). This phenomenon rationalizes the steady state ECL emission with the higher onset potential (resembling the $I_{ECL,Ru}$-E plot of the $[Ru(bpy)_3]^{2+}$/TPrA system) at faster k_{fcat} rates.

In addition to influencing the ECL intensity, reaction (*1.1*) also regulates the expansion of TPrA radicals into the solution. Consequently, the rate of homogeneous oxidation should profoundly affect the expansion of the $[Ru(bpy)_3]^{2+}$ ECL layer. We examined this influence by simulating the concentration profiles of $TPrA^{\bullet}$ and $[Ir^{IV}(sppy)_3]^{2-}$, along with the thickness of the ECL layer at 620 nm at different k_{fcat} values (Fig. S15). As expected, an increase in k_{fcat} results in a broader expansion of the $TPrA^{\bullet}$ concentration profile in the solution (Fig. S15A). However, it simultaneously restricts the diffusion layer of $[Ir^{IV}(sppy)_3]^{2-}$ species due to the redox catalysis process (to only 5 μm at $k_{fcat} = 3 \times 10^4\ M^{-1}s^{-1}$) (Fig. S15B). While $TPrA^{\bullet}$ governs the production of $[Ru(bpy)_3]^{+}$ in the solution, the concentration and distribution of suitable oxidants (in this case, $TPrA^{\bullet+}$ and $[Ir^{IV}(sppy)_3]^{2-}$) control the generation of the $[Ru(bpy)_3]^{2+}$ ECL. This is reflected in the decreasing thickness of the ECL emitting layer at faster k_{fcat} (Fig. S15C).

To summarize, Fig. 5 illustrates the intricate role of all reaction rates on the spatial distribution of the different intermediates involved. Focusing particularly on the electrocatalytic ECL pathway, at low potentials which relies on the inter-catalyst exchange rate, Ru^{+} species and ECL must be produced in regions rich in both $TPrA^{\bullet}$ and $[Ir^{IV}(sppy)_3]^{2-}$. By increasing k_{cat} the $[Ir^{IV}(sppy)_3]^{2-}$-rich region is more and more confined toward the electrode surface, decreasing its overlap with the $TPrA^{\bullet}$-rich region, which expands in solution. This makes the electrocatalytic pathway for ECL, at low potentials, less efficient with an ECL signal being shifted towards more positive potentials.

3.6. ECL of $[Ir^{III}(sppy)_3]^{3-}$/$[Ru(bpy)_3]^{2+}$/TPrA coreactant system

This exploratory study shows how the different homogeneous reactions govern the ECL profiles in terms of intensity, potential and spatial distribution. In the final phase of our study, we conducted numerical simulations aiming to replicate the experimentally observed variations in ECL intensity with potential at 515 nm and 620 nm for the $[Ru(bpy)_3]^{2+}$/TPrA, $[Ir^{III}(sppy)_3]^{3-}$/TPrA and $[Ir^{III}(sppy)_3]^{3-}$/$[Ru(bpy)_3]^{2+}$/TPrA coreactant systems (Fig. 6B). Although the simulated plots do not perfectly match the experimental data, they exhibit a reasonable degree of correlation in terms of onset potential, peak potential, and ECL intensity. However, this correlation is different among the systems. For the $[Ru(bpy)_3]^{2+}$/TPrA the simulation predicts ECL behavior that is in overall agreement with the experimental results (at least up to the peak potential, as shown in Fig. 3 and red plots in Fig. 6B). It is not the case for the other two systems which, while following the general experimental trends, align less well with the experimental I_{ECL}-E plots in terms of ECL onset and peak potential values.

The simulated $[Ir^{III}(sppy)_3]^{3-}$ ECL intensity, $I_{ECL,Ir}$, versus potential plot at 515 nm (light green) is identical for both the $[Ir^{III}(sppy)_3]^{3-}$/TPrA and $[Ir^{III}(sppy)_3]^{3-}$/$[Ru(bpy)_3]^{2+}$/TPrA coreactant systems. While its ECL onset potential aligns well with the experimental ones, the

maximal ECL intensity in the simulated plot is shifted to higher potentials and the overall shape of the ECL intensity versus potential plot deviates from the experimentally obtained ones. This disparity highlights that, while we have a good grasp of the fundamental reaction steps generating $[Ir^{III}(sppy)_3]^{3-}$ ECL, there is a need for a deeper understanding of their kinetics and of any side reactions contributing to the observed differences.

Moreover, it is noteworthy that the $[Ir^{III}(sppy)_3]^{3-}$ ECL intensity at 515 nm differs in Figs. 4 and 6B. Initially, in Fig. 4, our simulation predicted a significantly higher ECL intensity than what was observed in the experiment. This points toward the low coreactant efficiency of $[Ir^{III}(sppy)_3]^{3-}$ ECL generation, or might indicate that nonradiative decay plays a more significant role than we originally anticipated. To reproduce the experimentally obtained ECL intensity, we incorporated the reaction for non-emissive decay of the $[Ir^{III}(sppy)_3]^{3-*}$ into the model (reaction (*7.1*)) with a rate constant of $4.5 \times 10^9\ s^{-1}$.

$$\left[Ir(sppy)_3\right]^{3-*} \rightarrow \left[Ir(sppy)_3\right]^{3-} \tag{7.1}$$

Finally, the simulated $I_{ECL,Ru}$-E plot for $[Ru(bpy)_3]^{2+}$ ECL at 620 nm (Fig. 6B, orange plot) in the mixed luminophore/coreactant system is shifted to around 50 mV lower overpotential compared with the experimental one. The ECL generation in this system is complex and depends on multiple chemical steps, as shown in the previous section. While all of them contribute to the final ECL intensity, we reduced the number of reactions responsible for the lower ECL onset potential to only three. As previously discussed, the redox catalysis, the inter-Ir-Ru species redox-mediated $[Ru(bpy)_3]^{+}$ oxidation, and the reaction that generates $[Ir^{III}(sppy)_3]^{3-}$ ECL affect the onset ECL potential of $[Ru(bpy)_3]^{2+}$ in a way illustrated in Figs. 5B, 5A and S10C, respectively. Notably, varying those parameters led to simulated plots that can accurately replicate the experimental results, but further experimental information is needed to fully understand the nature of the reaction steps and their contribution to the chemistry of this complex coreactant system.

In broader terms, the here-developed model provides useful insights into the mechanism of the mixed luminophore coreactant system, but more importantly, it sparks discussion regarding the significance of specific mechanistic steps and the chemical properties of the mediator, particularly its redox properties, which can contribute to future research aimed at improving ECL signals. However, given the complexity of the mechanisms underlying the mixed luminophore system, the model remains under-characterised. In the future, efforts to delve into the reactivity and fine interplay of the kinetically limited mechanistic steps, and experimentation towards estimating the thickness of the ECL emitting layer [79,80], especially when varying the ratio of the components within this coreactant system, would greatly aid in this endeavour.

4. Conclusion

We have evaluated the crucial role of redox mediators in shaping ECL emission within the $[Ru(bpy)_3]^{2+}$/TPrA coreactant system, highlighting how the rate limiting processes involving the electrooxidized form of the Ir(III) mediator influence the efficiency of ECL emission, particularly at low electrode potentials. Specifically, we have demonstrated that to effectively enhance $[Ru(bpy)_3]^{2+}$ ECL emission at low anodic potentials, the redox mediator needs to mediate oxidation of both the coreactant and $[Ru(bpy)_3]^{+}$, as depicted in Fig. 6A. The former enables triggering the production of the coreactant reactive intermediates ($TPrA^{\bullet+}$ and $TPrA^{\bullet}$) at electrode potentials lower than those of their direct oxidation. The later provides a supplemental efficient path to produce the excited $[Ru(bpy)_3]^{2+*}$ luminophore.

For those two mediated oxidations to occur, specific conditions are required regarding the redox properties of the mediator compared to $[Ru(bpy)_3]^{2+}$ and the coreactant (see Fig. 6A). First, typically the mediator should have a standard potential higher than the $[Ru(bpy)_3]^{2+*}/[Ru(bpy)_3]^{+}$ couple and lower then, but close to, the coreactant oxidation. For the $[Ru(bpy)_3]^{+}$/TPrA system it should be between 0.6 and ca. 0.9 V. Secondly, the enhancement of ECL was shown to be more efficient if, unlike the $[Ru(bpy)_3]^{2+}$ luminophore, the redox mediator was not reduced by the $TPrA^{\bullet}$ radical. It is the case here, as the reduction of the $[Ir^{III}(sppy)_3]^{3-}$ redox mediator occurs at – 2.0 V vs Ag/AgCl, 0.4 V more negative than the $TPrA^{\bullet}$ oxidation potential.

In the present study, the redox mediator was also a luminophore, providing a second ECL signature. It was shown that this signature is also related to the redox mediation of the coreactant oxidation, meaning that the $[Ir^{III}(sppy)_3]^{3-}$ ECL takes places during the Ir complex oxidation. The simulation demonstrates that the $[Ir^{III}(sppy)_3]^{3-}$ ECL is also ruled by the redox properties of the $[Ir^{IV}(sppy)_3]^{2-}/[Ir^{III}(sppy)_3]^{3-*}$ couple and how it can participate in the redox conversion of both $TPrA^{\bullet}$ and $TPrA^{\bullet+}$ radical intermediates In particular, the thermodynamically infeasible reduction of $[Ir^{III}(sppy)_3]^{3-}$ restricts the generation of the $[Ir^{III}(sppy)_3]^{3-*}$ excited state to a single pathway: the homogeneous reduction of electrogenerated $[Ir^{IV}(sppy)_3]^{2-}$ by $TPrA^{\bullet}$, thereby limiting the $[Ir^{III}(sppy)_3]^{3-}$ ECL. Furthermore, by highlighting the quenching effect on $[Ru(bpy)_3]^{2+}$ ECL, induced by the oxidant ($[Ir^{IV}(sppy)_3]^{2-}$) scavenging the $TPrA^{\bullet}$ radicals, we suggest that the subsequent free radical reactivity should be further investigated.

Finally, we were able to reasonably reproduce the experimental ECL observations, and provide a mechanistic rationale of why the $[Ru(bpy)_3]^{2+}$ ECL occurs simultaneously with the oxidation of the redox mediator (and therefore at the same time as the $[Ir^{III}(sppy)_3]^{3-}$ ECL). This is of practical and analytical interest for ECL-based biosensors and bioassays because they would depend on the oxidation of an outer-sphere redox mediator, i.e. with a fast electron transfer kinetics, and no longer on the direct oxidation of the coreactant, which is much more dependent on the electrode nature and its passivation. This understanding not only advances our fundamental knowledge of ECL mechanisms but also prompts further experimentation, facilitating the development of ECL systems with tailored properties and improved performance.

CRediT authorship contribution statement

Sara Knežević: Writing – original draft, Visualization, Investigation, Formal analysis, Data curation. **Emily Kerr:** Investigation, Formal analysis, Data curation. **Giovanni Valenti:** Writing – review & editing, Validation, Methodology. **Francesco Paolucci:** Writing – review & editing, Supervision, Methodology, Funding acquisition. **Paul S. Francis:** Writing – review & editing, Validation, Supervision, Funding acquisition, Conceptualization. **Conor F. Hogan:** Writing – review & editing, Validation, Investigation. **Neso Sojic:** Writing – review & editing, Writing – original draft, Validation, Supervision, Funding acquisition, Conceptualization. **Frédéric Kanoufi:** Writing – review & editing, Writing – original draft, Validation, Supervision, Methodology, Funding acquisition, Formal analysis, Conceptualization.

Declaration of competing interest

The authors declare that they have no known competing financial interests or personal relationships that could have appeared to influence the work reported in this paper.

Data availability

I have added a link in the text (as a reference) to the academic repository where the data has been made available. Experimental data are available in AMS acta at https://doi.org/10.6092/unibo/amsacta/7697.

Acknowledgements

This work was supported by Agence Nationale de la Recherche (ELISE - ANR-21-CE42). This work was supported by ECLectic project that has received funding from the European Union's MSCA Doctoral Network Horizon Europe programme Grant Agreement Number 101119951.

Supplementary materials

Supplementary material associated with this article can be found, in the online version, at doi:10.1016/j.electacta.2024.144677.

References

[1] Z. Liu, W. Qi, G Xu, Recent advances in electrochemiluminescence, Chem. Soc. Rev. 44 (10) (2015) 3117–3142, https://doi.org/10.1039/C5CS00086F.
[2] X. Gou, Z. Xing, C. Ma, J.J. Zhu, A close look at mechanism, application, and opportunities of electrochemiluminescence microscopy, Chem. Biomed. Imaging 1 (5) (2023) 414–433, https://doi.org/10.1021/cbmi.2c00007.
[3] S. Knezevic, L. Bouffier, B. Liu, D. Jiang, N. Sojic, E.lectrochemiluminescence microscopy: from single objects to living cells, Curr. Opin. Electrochem. (2022) 101096, https://doi.org/10.1016/j.coelec.2022.101096.
[4] C. Meng, S. Knežević, F. Du, Y. Guan, F. Kanoufi, N. Sojic, G. Xu, Recent advances in electrochemiluminescence imaging analysis, eScience 2 (6) (2022) 591–605, https://doi.org/10.1016/j.esci.2022.10.004.
[5] W. Guo, H. Ding, C. Gu, Y. Liu, X. Jiang, B. Su, Y. Shao, Potential-resolved multicolor electrochemiluminescence for multiplex immunoassay in a single sample, J. Am. Chem. Soc. 140 (46) (2018) 15904–15915, https://doi.org/10.1021/jacs.8b09422.
[6] S. Rebeccani, C. Wetzl, V.A. Zamolo, A. Criado, G. Valenti, F. Paolucci, M. Prato, Electrochemiluminescent immunoassay enhancement driven by carbon nanotubes, Chem. Commun. 57 (76) (2021) 9672–9675, https://doi.org/10.1039/D1CC03457J.
[7] A. Zanut, F. Palomba, M. Rossi Scota, S. Rebeccani, M. Marcaccio, D. Genovese, E. Rampazzo, G. Valenti, F. Paolucci, L Prodi, Dye-doped silica nanoparticles for enhanced ECL-based immunoassay analytical performance, Angew. Chem. Int. Ed. 59 (49) (2020) 21858–21863, https://doi.org/10.1002/anie.202009544.
[8] Y. Wang, R. Jin, N. Sojic, D. Jiang, H. Chen, Intracellular wireless analysis of single cells by bipolar electrochemiluminescence confined in a nanopipette, Angew. Chem. Int. Ed. 59 (26) (2020) 10416–10420, https://doi.org/10.1002/anie.202002323.
[9] Y. Chen, Y. Xiang, R. Yuan, Y. Chai, A restriction enzyme-powered autonomous DNA walking machine: its application for a highly sensitive electrochemiluminescence assay of DNA, Nanoscale 7 (3) (2014) 981–986, https://doi.org/10.1039/C4NR05387G.
[10] Z. Xu, Y. Dong, J. Li, R Yuan, A ferrocene-switched electrochemiluminescence "off–on" strategy for the sensitive detection of cardiac troponin i based on target transduction and a DNA walking machine, Chem. Commun. 51 (76) (2015) 14369–14372, https://doi.org/10.1039/C5CC04745E.
[11] L. Yang, Y. Tao, G. Yue, R. Li, B. Qiu, L. Guo, Z. Lin, H.H. Yang, Highly selective and sensitive electrochemiluminescence biosensor for P53 DNA sequence based on nicking endonuclease assisted target recycling and hyperbranched rolling circle amplification, Anal. Chem. 88 (10) (2016) 5097–5103, https://doi.org/10.1021/acs.analchem.5b04521.
[12] G. Valenti, S. Scarabino, B. Goudeau, A. Lesch, M. Jović, E. Villani, M. Sentic, S. Rapino, S. Arbault, F. Paolucci, N. Sojic, Single cell electrochemiluminescence imaging: from the proof-of-concept to disposable device-based analysis, J. Am. Chem. Soc. 139 (46) (2017) 16830–16837, https://doi.org/10.1021/jacs.7b09260.
[13] S. Voci, B. Goudeau, G. Valenti, A. Lesch, M. Jović, S. Rapino, F. Paolucci, S. Arbault, N Sojic, Surface-confined electrochemiluminescence microscopy of cell membranes, J. Am. Chem. Soc. 140 (44) (2018) 14753–14760, https://doi.org/10.1021/jacs.8b08080.
[14] S. Knežević, E. Kerr, B. Goudeau, G. Valenti, F. Paolucci, P.S. Francis, F. Kanoufi, N Sojic, Bimodal electrochemiluminescence microscopy of single cells, Anal. Chem. 95 (18) (2023) 7372–7378, https://doi.org/10.1021/acs.analchem.3c00869.
[15] H. Ding, W. Guo, B Su, Imaging cell-matrix adhesions and collective migration of living cells by electrochemiluminescence microscopy, Angew. Chem. Int. Ed. 59 (1) (2020) 449–456, https://doi.org/10.1002/anie.201911190.
[16] H. Ding, P. Zhou, W. Fu, L. Ding, W. Guo, B Su, Spatially selective imaging of cell–matrix and cell–cell junctions by electrochemiluminescence, Angew. Chem. Int. Ed. 60 (21) (2021) 11769–11773, https://doi.org/10.1002/anie.202101467.
[17] J. Dong, Y. Lu, Y. Xu, F. Chen, J. Yang, Y. Chen, J. Feng, Direct imaging of single-molecule electrochemical reactions in solution, Nature 596 (7871) (2021) 244–249, https://doi.org/10.1038/s41586-021-03715-9.
[18] J. Dong, Y. Xu, Z. Zhang, J Feng, Operando imaging of chemical activity on gold plates with single-molecule electrochemiluminescence microscopy, Angew. Chem. Int. Ed. 61 (14) (2022) e202200187, https://doi.org/10.1002/anie.202200187.
[19] Y. Liu, H. Zhang, B. Li, J. Liu, D. Jiang, B. Liu, N. Sojic, Single biomolecule imaging by electrochemiluminescence, J. Am. Chem. Soc. 143 (43) (2021) 17910–17914, https://doi.org/10.1021/jacs.1c06673.
[20] P.A. Defnet, B. Zhang, Detection of transient nanoparticle collision events using electrochemiluminescence on a closed bipolar microelectrode, ChemElectroChem 7 (1) (2020) 252–259, https://doi.org/10.1002/celc.201901734.
[21] F.R.F. Fan, A.J. Bard, Observing single nanoparticle collisions by electrogenerated chemiluminescence amplification, Nano Lett 8 (6) (2008) 1746–1749, https://doi.org/10.1021/nl8009236.
[22] J.E. Dick, C. Renault, B.K. Kim, A.J. Bard, Simultaneous detection of single attoliter droplet collisions by electrochemical and electrogenerated chemiluminescent responses, Angew. Chem. Int. Ed. 53 (44) (2014) 11859–11862, https://doi.org/10.1002/anie.201407937.
[23] Y.B. Vogel, C.W. Evans, M. Belotti, L. Xu, I.C. Russell, L.J. Yu, A.K.K. Fung, N. S. Hill, N. Darwish, V.R. Gonçales, M.L. Coote, K. Swaminathan Iyer, S. Ciampi, The corona of a surface bubble promotes electrochemical reactions, Nat. Commun. 11 (1) (2020) 6323, https://doi.org/10.1038/s41467-020-20186-0.
[24] M.W. Glasscott, J.E. Dick, Visualizing phase boundaries with electrogenerated chemiluminescence, J. Phys. Chem. Lett. 11 (12) (2020) 4803–4808, https://doi.org/10.1021/acs.jpclett.0c01207.
[25] M.W. Glasscott, S. Voci, P.J. Kauffmann, A.I. Chapoval, J.E. Dick, Mapping solvent entrapment in multiphase systems by electrogenerated chemiluminescence, Langmuir 37 (9) (2021) 2907–2912, https://doi.org/10.1021/acs.langmuir.0c03445.
[26] M.M. Chen, C.H. Xu, W. Zhao, H.Y. Chen, J.J. Xu, Observing the structure-dependent electrocatalytic activity of bimetallic Pd–Au nanorods at the single-particle level, Chem. Commun. 56 (23) (2020) 3413–3416, https://doi.org/10.1039/D0CC00185F.
[27] Y. Chen, D. Zhao, J. Fu, X. Gou, D. Jiang, H. Dong, J.J. Zhu, In situ imaging facet-induced spatial heterogeneity of electrocatalytic reaction activity at the subparticle level via electrochemiluminescence microscopy, Anal. Chem 91 (10) (2019) 6829–6835, https://doi.org/10.1021/acs.analchem.9b01044.
[28] H. Zhu, D. Jiang, J.J. Zhu, High-resolution imaging of catalytic activity of a single graphene sheet using electrochemiluminescence microscopy, Chem. Sci. 12 (13) (2021) 4794–4799, https://doi.org/10.1039/D0SC06967A.
[29] S. Rebeccani, A. Zanut, C.I. Santo, G. Valenti, F. Paolucci, A guide inside electrochemiluminescent microscopy mechanisms for analytical performance improvement, Anal. Chem. 94 (1) (2022) 336–348, https://doi.org/10.1021/acs.analchem.1c05065.
[30] W. Miao, J.P. Choi, A.J. Bard, Electrogenerated chemiluminescence 69: The Tris (2,2'-Bipyridine)ruthenium(II), (Ru(Bpy)32+)/Tri-n-propylamine (TPrA) system revisiteda new route involving TPrA•+ cation radicals, J. Am. Chem. Soc. 124 (48) (2002) 14478–14485, https://doi.org/10.1021/ja027532v.
[31] A. Zanut, A. Fiorani, S. Canola, T. Saito, N. Ziebart, S. Rapino, S. Rebeccani, A. Barbon, T. Irie, H.P. Josel, F. Negri, M. Marcaccio, M. Windfuhr, K. Imai, G. Valenti, F Paolucci, Insights into the mechanism of coreactant electrochemiluminescence facilitating enhanced bioanalytical performance, Nat. Commun. 11 (1) (2020) 2668, https://doi.org/10.1038/s41467-020-16476-2.
[32] P. Nikolaou, G. Valenti, F. Paolucci, Nano-structured materials for the electrochemiluminescence signal enhancement, Electrochim. Acta 388 (2021) 138586, https://doi.org/10.1016/j.electacta.2021.138586.
[33] A. Fiorani, J.P. Merino, A. Zanut, A. Criado, G. Valenti, M. Prato, F. Paolucci, Advanced carbon nanomaterials for electrochemiluminescent biosensor applications, Curr. Opin. Electrochem. 16 (2019) 66–74, https://doi.org/10.1016/j.coelec.2019.04.018.
[34] S. Kesarkar, S. Valente, A. Zanut, F. Palomba, A. Fiorani, M. Marcaccio, E. Rampazzo, G. Valenti, F. Paolucci, L. Prodi, Neutral dye-doped silica nanoparticles for electrogenerated chemiluminescence signal amplification, J. Phys. Chem. C 123 (9) (2019) 5686–5691, https://doi.org/10.1021/acs.jpcc.8b11049.
[35] P. Dai, C. Liu, C. Xie, J. Ke, Y. He, L. Wei, L. Chen, J. Jin, TiO2 nanotubes loaded with CdS nanocrystals as enhanced emitters of electrochemiluminescence: application to an assay for prostate-specific antigen, Anal Bioanal Chem 412 (6) (2020) 1375–1384, https://doi.org/10.1007/s00216-019-02365-1.
[36] A. Abdussalam, G. Xu, Recent advances in electrochemiluminescence luminophores, Anal Bioanal Chem 414 (1) (2022) 131–146, https://doi.org/10.1007/s00216-021-03329-0.
[37] F. Rizzo, F. Polo, G. Bottaro, S. Fantacci, S. Antonello, L. Armelao, S. Quici, F. Maran, From blue to green: fine-tuning of photoluminescence and electrochemiluminescence in bifunctional organic dyes, J. Am. Chem. Soc. 139 (5) (2017) 2060–2069, https://doi.org/10.1021/jacs.6b12247.
[38] G.J. Barbante, E.H. Doeven, E. Kerr, T.U. Connell, P.S. Donnelly, J.M. White, T. Lópes, S. Laird, D.J.D. Wilson, P.J. Barnard, C.F. Hogan, P.S. Francis, Understanding electrogenerated chemiluminescence efficiency in blue-shifted Iridium(III)-complexes: an experimental and theoretical study, Eur. J. Chem. 20 (12) (2014) 3322–3332, https://doi.org/10.1002/chem.201304500.
[39] D. Bruce, M.M. Richter, Green Electrochemiluminescence from ortho-metalated tris(2-Phenylpyridine)Iridium(III), Anal. Chem. 74 (6) (2002) 1340–1342, https://doi.org/10.1021/ac0111513.
[40] L. Chen, D.J. Hayne, E.H. Doeven, J. Agugiaro, D.J.D. Wilson, L.C. Henderson, T. U. Connell, Y.H. Nai, R. Alexander, S. Carrara, C.F. Hogan, P.S. Donnelly, P. S. Francis, A conceptual framework for the development of Iridium(III) complex-based electrogenerated chemiluminescence labels, Chem. Sci. 10 (37) (2019) 8654–8667, https://doi.org/10.1039/C9SC01391A.
[41] M.A. Haghighatbin, S.E. Laird, C.F. Hogan, Electrochemiluminescence of cyclometalated Iridium (III) complexes, Curr. Opin. Electrochem 7 (2018) 216–223, https://doi.org/10.1016/j.coelec.2018.03.026.
[42] S.A. Kitte, C. Wang, S. Li, Y. Zholudov, L. Qi, J. Li, G. Xu, Electrogenerated Chemiluminescence of Tris(2,2'-Bipyridine)ruthenium(II) Using N-(3-

Aminopropyl)diethanolamine as coreactant, Anal Bioanal Chem 408 (25) (2016) 7059–7065, https://doi.org/10.1007/s00216-016-9409-z.
[43] H. Xing, Q. Zhai, X. Zhang, J. Li, E. Wang, Boron nitride quantum dots as efficient coreactant for enhanced electrochemiluminescence of ruthenium(II) Tris(2,2′-Bipyridyl), Anal. Chem. 90 (3) (2018) 2141–2147, https://doi.org/10.1021/acs.analchem.7b04428.
[44] C.V. Raju, S.S. Kumar, Highly sensitive novel cathodic electrochemiluminescence of Tris(2,2′-Bipyridine)Ruthenium(II) using glutathione as a co-reactant, Chem. Commun. 53 (49) (2017) 6593–6596, https://doi.org/10.1039/C7CC03349D.
[45] F. Yuan, M.I. Halawa, X. Ma, A. Abdussalam, B. Lou, G. Xu, Electrochemiluminescence of Ru(Bpy)32+/Oxamic Hydrazide and Its Application for Selective Detection of 4-Nitrobenzaldehyde, ChemElectroChem 7 (20) (2020) 4239–4244, https://doi.org/10.1002/celc.202001140.
[46] E. Daviddi, A. Oleinick, I. Svir, G. Valenti, F. Paolucci, C. Amatore, Theory and simulation for optimising electrogenerated chemiluminescence from Tris(2,2′-Bipyridine)-Ruthenium(II)-doped silica nanoparticles and tripropylamine, ChemElectroChem 4 (7) (2017) 1719–1730, https://doi.org/10.1002/celc.201600892.
[47] J. Ding, P. Zhou, B. Su, Quantum efficiency of electrochemiluminescence generation by Tris(2,2'-Bipyridine)Ruthenium(II) and Tri-n-Propylamine revisited from a kinetic reaction model, ChemElectroChem 9 (12) (2022) e202200236, https://doi.org/10.1002/celc.202200236.
[48] O.V. Klymenko, I. Svir, C. Amatore, A new approach for the simulation of electrochemiluminescence (ECL), ChemPhysChem 14 (10) (2013) 2237–2250, https://doi.org/10.1002/cphc.201300126.
[49] W.X. Fu, P. Zhou, W.L. Guo, B. Su, Imaging electrochemiluminescence layer to dissect concentration-dependent light intensity for accurate quantitative analysis, Adv. Sens. Energy Mater. 1 (3) (2022) 100028, https://doi.org/10.1016/j.asems.2022.100028.
[50] B.D. Muegge, M.M. Richter, Multicolored electrogenerated chemiluminescence from ortho-metalated Iridium(III) systems, Anal. Chem. 76 (1) (2004) 73–77, https://doi.org/10.1021/ac035038j.
[51] S. Zanarini, M. Felici, G. Valenti, M. Marcaccio, L. Prodi, S. Bonacchi, P. Contreras-Carballada, R.M. Williams, M.C. Feiters, R.J.M. Nolte, L. De Cola, F. Paolucci, Green and blue electrochemically generated chemiluminescence from click chemistry—customizable iridium complexes, Eur. J. Chem. 17 (16) (2011) 4640–4647, https://doi.org/10.1002/chem.201002956.
[52] A. Kapturkiewicz, Cyclometalated Iridium(III) chelates—a new exceptional class of the electrochemiluminescent luminophores, Anal. Bioanal. Chem. 408 (25) (2016) 7013–7033, https://doi.org/10.1007/s00216-016-9615-8.
[53] Q. Zhao, M. Yu, L. Shi, S. Liu, C. Li, M. Shi, Z. Zhou, C. Huang, F. Li, Cationic Iridium(III) complexes with tunable emission color as phosphorescent dyes for live cell imaging, Organometallics 29 (5) (2010) 1085–1091, https://doi.org/10.1021/om900691r.
[54] E. Kerr, E.H. Doeven, G.J. Barbante, T.U. Connell, P.S. Donnelly, D.J.D. Wilson, T. D. Ashton, F.M. Pfeffer, P.S.Blue Francis, Electrogenerated chemiluminescence from water-soluble iridium complexes containing sulfonated phenylpyridine or tetraethylene glycol derivatized triazolylpyridine ligands, Eur. J. Chem. 21 (42) (2015) 14987–14995, https://doi.org/10.1002/chem.201502037.
[55] E. Kerr, D.J. Hayne, L.C. Soulsby, J.C. Bawden, S.J. Blom, E.H. Doeven, L. C. Henderson, C.F. Hogan, P.S. Francis, A redox-mediator pathway for enhanced multi-colour electrochemiluminescence in aqueous solution, Chem. Sci. 13 (2) (2022) 469–477, https://doi.org/10.1039/D1SC05609C.
[56] E. Kerr, S. Knezevic, P.S. Francis, C.F. Hogan, G. Valenti, F. Paolucci, F. Kanoufi, N. Sojic, Electrochemiluminescence amplification in bead-based assays induced by a freely diffusing Iridium(III) complex, ACS Sens 8 (2) (2023) 933–939, https://doi.org/10.1021/acssensors.2c02697.
[57] A. Fracassa, C.I. Santo, E. Kerr, S. Knežević, D.J. Hayne, P.S. Francis, F. Kanoufi, N. Sojic, F. Paolucci, G. Valenti, Redox-mediated electrochemiluminescence enhancement for bead-based immunoassay, Chem. Sci. (2023), https://doi.org/10.1039/D3SC06357G.
[58] S.J. Blom, N.S. Adamson, E. Kerr, E.H. Doeven, O.S. Wenger, R.S. Schaer, D. J. Hayne, F. Paolucci, N. Sojic, G. Valenti, P.S.Redox Francis, Mediated enhancement and quenching of co-reactant electrochemiluminescence by Iridium (III) complexes, Electrochim. Acta 484 (2024) 143957, https://doi.org/10.1016/j.electacta.2024.143957.
[59] C. Costentin, M. Robert, J.M. Savéant, Catalysis of the electrochemical reduction of carbon dioxide, Chem. Soc. Rev. 42 (6) (2013) 2423–2436, https://doi.org/10.1039/C2CS35360A.
[60] C. Costentin, J.M Savéant, Multielectron, multistep molecular catalysis of electrochemical reactions: benchmarking of homogeneous catalysts, ChemElectroChem 1 (7) (2014) 1226–1236, https://doi.org/10.1002/celc.201300263.
[61] X. Guo, Y. Okamoto, M.R. Schreier, T.R. Ward, O.S. Wenger, Enantioselective synthesis of amines by combining photoredox and enzymatic catalysis in a cyclic reaction network, Chem. Sci. 9 (22) (2018) 5052–5056, https://doi.org/10.1039/C8SC01561A.
[62] S. Knežević, F.ECLectic Kanoufi, WP2 Electrochemiluminescence mechanism performance optimisation. T2.1 optimization reagents, University of Bologna, 2024. March, https://amsacta.unibo.it/id/eprint/7697/.
[63] M. Sentic, M. Milutinovic, F. Kanoufi, D. Manojlovic, S. Arbault, N. Sojic, Mapping electrogenerated chemiluminescence reactivity in space: mechanistic insight into model systems used in immunoassays, Chem. Sci. 5 (6) (2014) 2568–2572, https://doi.org/10.1039/C4SC00312H.
[64] D. Han, D. Fang, G. Valenti, F. Paolucci, F. Kanoufi, D. Jiang, N. Sojic, Dynamic mapping of electrochemiluminescence reactivity in space: application to bead-based assays, Anal. Chem. 95 (42) (2023) 15700–15706, https://doi.org/10.1021/acs.analchem.3c02960.
[65] M.J. Chalkley, P. Garrido-Barros, J.C. Peters, A Molecular mediator for reductive concerted proton-electron transfers via electrocatalysis, Science 369 (6505) (2020) 850–854, https://doi.org/10.1126/science.abc1607.
[66] R. Deeba, S. Chardon-Noblat, C. Costentin, Homogeneous molecular catalysis of the electrochemical reduction of N 2 O to N 2 : redox vs. Chemical catalysis, Chem. Sci. 12 (38) (2021) 12726–12732, https://doi.org/10.1039/D1SC03044B.
[67] D.J. Martin, C.F. Wise, M.L. Pegis, J.M. Mayer, Developing scaling relationships for molecular electrocatalysis through studies of fe-porphyrin-catalyzed O2 reduction, Acc. Chem. Res. 53 (5) (2020) 1056–1065, https://doi.org/10.1021/acs.accounts.0c00044.
[68] C. Costentin, S. Drouet, M. Robert, J.M. Savéant, Turnover numbers, turnover frequencies, and overpotential in molecular catalysis of electrochemical reactions. cyclic voltammetry and preparative-scale electrolysis, J. Am. Chem. Soc. 134 (27) (2012) 11235–11242, https://doi.org/10.1021/ja303560c.
[69] R.Y. Lai, A.J. Bard, Electrogenerated Chemiluminescence. 70. The application of ECL to determine electrode potentials of Tri-n-propylamine, its radical cation, and intermediate free radical in MeCN/benzene solutions, J. Phys. Chem. A 107 (18) (2003) 3335–3340, https://doi.org/10.1021/jp026743j.
[70] F. Kanoufi, Y. Zu, A.J. Bard, Homogeneous oxidation of trialkylamines by metal complexes and its impact on electrogenerated chemiluminescence in the trialkylamine/Ru(Bpy)32+ system, J. Phys. Chem. B 105 (1) (2001) 210–216, https://doi.org/10.1021/jp002880+.
[71] Y. Zu, A.J. Bard, Electrogenerated chemiluminescence. 66. the role of direct coreactant oxidation in the ruthenium tris(2,2‘)Bipyridyl/tripropylamine system and the effect of halide ions on the emission intensity, Anal. Chem. 72 (14) (2000) 3223–3232, https://doi.org/10.1021/ac000199y.
[72] Z. Chen, Y. Zu, Electrogenerated chemiluminescence of the Tris(2,2′-Bipyridine) ruthenium(II)/Tri-n-propylamine (TPrA) system: crucial role of the long lifetime of tpra•+ cation radicals suggested by electrode surface effects, J. Phys. Chem. C 112 (42) (2008) 16663–16667, https://doi.org/10.1021/jp802873e.
[73] K. Imai, G. Valenti, E. Villani, S. Rapino, E. Rampazzo, M. Marcaccio, L. Prodi, F. Paolucci, Numerical simulation of doped silica nanoparticle electrochemiluminescence, J. Phys. Chem. C 119 (46) (2015) 26111–26118, https://doi.org/10.1021/acs.jpcc.5b07107.
[74] E.H. Doeven, E.M. Zammit, G.J. Barbante, P.S. Francis, N.W. Barnett, C.F. Hogan, A potential-controlled switch on/off mechanism for selective excitation in mixed electrochemiluminescent systems, Chem. Sci. 4 (3) (2013) 977–982, https://doi.org/10.1039/C2SC21707D.
[75] E. Kerr, E.H. Doeven, D.J.D. Wilson, C.F. Hogan, P.S. Francis, Considering the chemical energy requirements of the tri-n-propylamine co-reactant pathways for the judicious design of new electrogenerated chemiluminescence detection systems, Analyst 141 (1) (2016) 62–69, https://doi.org/10.1039/C5AN01462J.
[76] J.M. Fernandez-Hernandez, E. Longhi, R. Cysewski, F. Polo, H.P. Josel, L. De Cola, Photophysics and electrochemiluminescence of bright cyclometalated Ir(III) complexes in aqueous solutions, Anal. Chem. 88 (8) (2016) 4174–4178, https://doi.org/10.1021/acs.analchem.6b00312.
[77] E. Longhi, J.M. Fernandez-Hernandez, A. Iordache, R. Fröhlich, H.P. Josel, L. De Cola, Ir(III) cyclometalated complexes containing phenylphenanthridine ligands with different substitutions: effects on the electrochemiluminescence properties, Inorg. Chem. 59 (11) (2020) 7435–7443, https://doi.org/10.1021/acs.inorgchem.0c00107.
[78] W. Guo, P. Zhou, L. Sun, H. Ding, B. Su, Microtube electrodes for imaging the electrochemiluminescence layer and deciphering the reaction mechanism, Angew. Chem. Int. Ed. 60 (4) (2021) 2089–2093, https://doi.org/10.1002/anie.202012340.
[79] Y. Wang, W. Guo, Q. Yang, B. Su, Electrochemiluminescence self-interference spectroscopy with vertical nanoscale resolution, J. Am. Chem. Soc. 142 (3) (2020) 1222–1226, https://doi.org/10.1021/jacs.9b12833.
[80] Y. Wang, J. Ding, P. Zhou, J. Liu, Z. Qiao, K. Yu, J. Jiang, B. Su, Electrochemiluminescence distance and reactivity of coreactants determine the sensitivity of bead-based immunoassays, Angew. Chem. Int. Ed. 62 (16) (2023) e202216525, https://doi.org/10.1002/anie.202216525.